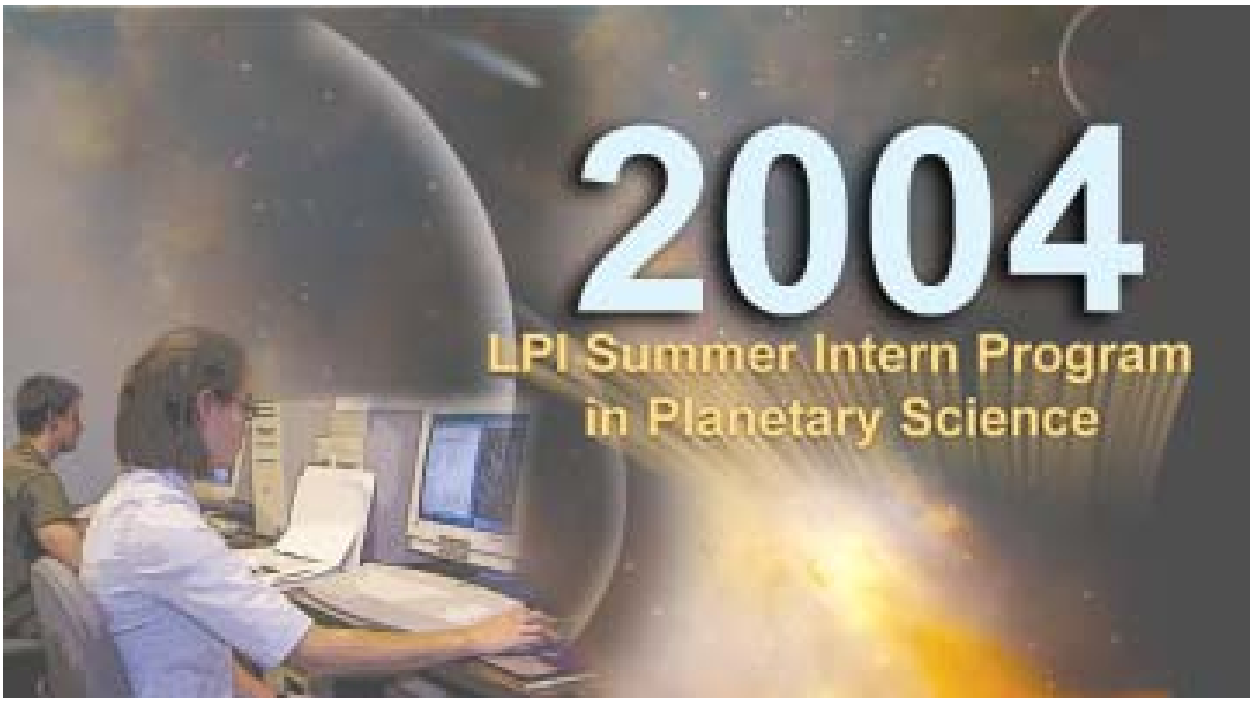

Papers Presented at the

20th annual

Summer Intern Conference

August 12, 2004 — Houston, Texas

Papers Presented at the

Twentieth Annual
SUMMER INTERN CONFERENCE

August 12, 2004
Houston, Texas

2004 Summer Intern Program for Undergraduates
Lunar and Planetary Institute

Sponsored by
Lunar and Planetary Institute
NASA Johnson Space Center

Compiled in 2004 by

Publications and Program Services Department
Lunar and Planetary Institute
3600 Bay Area Boulevard
Houston TX 77058-1113, USA

The Lunar and Planetary Institute is operated by the Universities Space Research Association and supported by the National Aeronautics and Space Administration under Cooperative Agreement No. NCC5-679 issued through the Solar System Exploration Division.

AGENDA

8:00 Breakfast in LPI Great Room

INTERN PRESENTATIONS
Chair: Dr. Julie Moses

8:30 Opening statements by LPI Director, Dr. Stephen Mackwell

* **EMILY BJONNES, Rutgers University** (Advisor: J. Lindsay)
3.54 Billion Year-Old Cherts from Western Australia: Were They Formed by Living Organisms?

8:40 **BRIAN BUE, Augsburg College** (Advisor: T. Stepinski)
Automated Classification of Martian Topographical Data

9:00 **SARAH COLLINS, Imperial College of Science, Technology and Medicine** (Advisors: K. Righter and A. Brandon)
Mineralogy and Petrology of Lunar Mare Basalts LAP 02205, LAP 02226, LAP 02224 and LAP 02436

9:20 **SELBY CULL, Hampshire College** (Advisors: P. McGovern and A. Treiman)
Evidence for Extensive Fluvial Erosion Around Olympus Mons: A Multi-Resolution Survey

9:40 **HEATHER DALTON, Stephen F. Austin State University** (Advisors: D. Musselwhite and A. Treiman)
Experimental Petrology of the New Martian Meteorite Yamato 980459

10:00 **NICHOLAS HEAVENS, University of Chicago** (Advisor: L. Kirkland)
Field Experience for Mars Exploration via Infrared Spectrometers

10:20 **JARED HOWENSTINE, University of Massachusetts Amherst** (Advisor: W. Kiefer)
Topographic Study of Large Martian Impact Craters

10:40 *Break*

11:00 **YOKO KEBUKAWA, Tokyo Institute of Technology** (Advisor: M. Zolensky)
Search for Fluid Inclusions in Meteorites and Initial Characterization

11:20 **SCOTT MCBRIDE, Cornell University** (Advisors: C. Allen and M. S. Bell)
Prospecting for Martian Ice

11:40 **TÁHIRIH MOTAZEDIAN, University of Oregon** (Advisor: K. Snook)
Iron Metal Spherules Found at Deep-Sea Hydrothermal Vent

12:00 **AKIKO SUZUKI, Kyushu University** (Advisor: L. Keller)
An Infrared Spectroscopy and Electron Microscopy Study of Antarctic Micrometeorites: Mineralogy and Organic Matter

12:20 Closing Remarks

12:35 ***Adjourn — Photos***

12:45 ***Lunch in LPI Great Room***

* *Talk was presented on July 30.*

CONTENTS

3.54 Billion-Year-Old Cherts from Western Australia: Were They Formed by Living Organisms?

Bjonnes, Emily E[1] and Lindsay, John F[2]. [1]Rutgers University, Dept Geological Sciences, Piscataway, NJ 08854. [2]Lunar and Planetary Institute, Houston, TX 77058

INTRODUCTION: The Pilbara Craton in Northwestern Australia is home to some of the oldest and least metamorphosed rocks on Earth. One example of such a group of rocks in this area is the 3.51 Ga Coucal Formation in the Coonterunah Group. The Coucal Formation, which is predominantly basalt with thin interbedded chert layers, is slightly over 700 m thick (Fig 1):

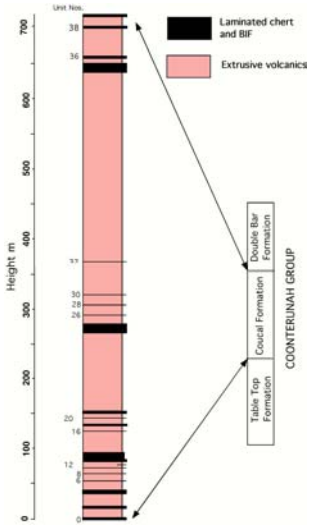

Fig 1: Stratigraphic section of the Coucal Formation.

The formation is underlain by the Table Top Formation and overlain by the Double Bar Formation, both of which are composed of metabasalt, metadolerite, and amphibolites [1]. Much of the geology above the Coucal Formation is thought to be hydrothermal in origin based on the rocks' textures and mineralogy [2]. This study investigates the origins of the cherts in the Coucal Formation.

METHODS: Hand samples and thin sections of the chert layers were first examined in macroscopically and then under a petrographic microscope. After locating promising textural associations in thin section, more work was carried out on the JEOL 5910LV Scanning Electron Microscope (SEM) at a potential of 15 kV. Thin sections were imaged either as backscatter electron (BSE) images (BEI) or scanning electron images (SEI) at various magnifications ranging from 90x to 1500x. Elemental data was collected using the SEM's X-ray Energy Dispersion Spectrum (EDS). The basalt analyses consisted of whole rock analysis done by X-ray fluorescence. We then used this data for making normative calculations for the basalt composition.

RESULTS: The basalts of the Coucal Formation are extrusive volcanics. They are fine grained and pillowed. Their compositions are relatively homogeneous, and the majority of the basalts are trachytes, trachyandesites, or trachybasalts based on normative calculations. Of the 17 basalt samples analyzed, four of them are very unexpectedly quartz rich. One sample falls in between these two extremes and is an alkali rhyolite based on the normative calculation (Fig 2). Sample, C28, was very quartz depleted and we were unable to identify the rock type based on chemistry.

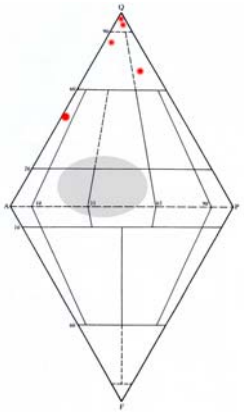

Fig 2: QAPF diagram showing distribution of basalt compositions. The shaded ellipse shows the majority of the compositions. The red dots are the unusual data points.

In addition to looking at the composition of the basalt and determining the rock type, we studied trace element data. By looking at the amounts of titanium and zirconium, it is possible to distinguish some petrographic origins of an igneous rock [3]. When the titanium and zirconium abundances of the Coucal Formations' basalts are plotted against each other, our data follows an ocean floor basalt trend (Fig 3).

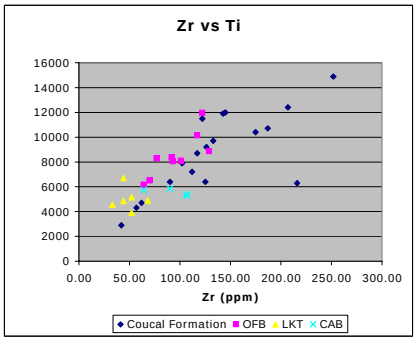

Fig 3: Plot showing the relationship between zirconium and titanium in various types of basaltic flows. Basalts from the Coucal formation (blue data points) most closely follow those of the Ocean Floor Basalts (OFB) whose points are shown in pink.

The main focus of this study was the chert layers interbedded in the basalt layers. They are composed predominantly of quartz (generally >98%) and have bands of iron oxides of varying thicknesses. Minerals such as hematite, magnetite, iron silicates, and aluminum silicates are found in the cherts throughout the Coucal Formation. Some of the more exotic minerals concentrated in the lower section of the formation include 10-100 m-wide grains of iron and magnesium silicates, titanium and iron sulfides, and magnesium oxides. The top of the Coucal Formation has a higher phosphorous and titanium content than the rest of the section. There were also significant trace elements found in several of the sections—evidence of zirconium, manganese, copper, and gold were found in some of the thin sections. These, along with many other trace elements, were found in ppm abundances in whole rock analyses of an adjacent formation.

Many of the cherts are massive and have sedimentary characteristics. The quartz in the chert is often mosaiced and has undulatory extinction. Much of the hematite in these sections is bladed and these blades often propagate radially (Fig 4):

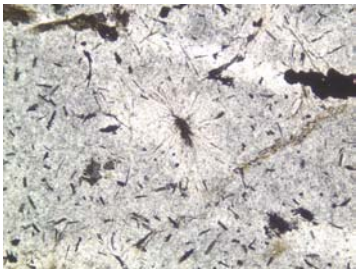

Fig 4: Transmitted-light (10x) photograph of section C02. In the center, one can clearly see a clump of hematite blades growing radially outward.

There are also gray bladed minerals that are possibly sillimanite but a conclusive analysis was not achieved. These blades grew radially from individual sources or the sides of opaque bands.

Perhaps the most visible sedimentary structures in the chert layers are in two samples, C17 and C20. The opaque bands in these samples are composed of small iron oxide spheres which appear to have settled together to form a layer (Fig 5). The spheres are all very nearly 10 m in diameter with very little variation. They appear densely packed towards the center of the opaque bands, but there are pockets of less densely packed spherules near the edges of the bands and rarely on the interior of the bands. The spheres have a hematite core surrounded by a magnetite shell, which is probably a product of alteration. The banding in the other samples suggests that a similar settling process may have worked throughout the formation.

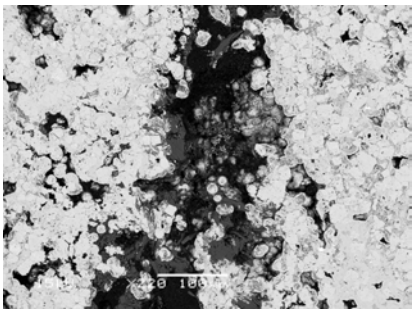

Fig 5: BSE image of sample C17 (220x). The small white spheres are composed of iron oxide. A crack runs through the center.

All of the chert sections from the Coucal Formation contain vugs, small fractures, and various types of veins. These indicate strong dissolution processes and stresses were working on the beds after deposition. Some of the holes in the sections have large opaques growing on the sides in a variety of shapes (Figs 6 and 7):

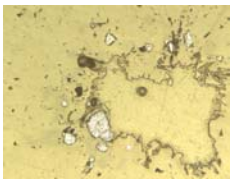

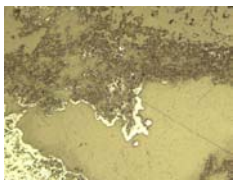

Figs 6 and 7: Reflected light images (10x) of sample C20 showing euhedral opaque grains and rounded, globular opaque grains growing on the edges of holes.

Some samples have veins which were then filled by minerals deposited later in the rocks' history. One sample, C13, has a large carbonate vein that may have formed this way. Nearly all of the samples are criss-crossed with quartz and opaque veins suggesting a long post-depositional history.

DISCUSSION: Many of the qualities found in Coucal Formation support the hypothesis that these rocks formed in a hydrothermal setting. The basalts are pillowed and show textures, mineralogy and trace element quantities expected of basalts erupted on the sea floor. This corresponds to a hydrothermal setting, as hydrothermal vents are often found very close to mid-ocean ridges where basalts are erupted directly onto the ocean floor.

The chert layers in the Coucal Formation also have indicators of a hydrothermal origin. The cherts contain traces of rare elements such as titanium and vanadium most often found in hydrothermal deposits [4]. Most notably, sample C34 has a small grain of gold. This is particularly interesting since gold deposits are often found in quartz veins within a hydrothermal

system. Gold also occurs widely on the Pilbara Craton in other geologic formations. The discovery of this gold grain along with other trace elements throughout the chert layers is good support for a hypothesis of a hydrothermal origin.

In addition to the trace elements found in some of the chert layers, minerals found throughout the formation provide clues to the origin of the chert and basalt. Calcium sulfate, which could be gypsum or anhydrite, was found in two of the chert thin sections towards the top of the formation. Iron sulfides and potassium compounds were also found in sample C02. These mineralogies are strong indicators of a hydrothermal environment. There are also some samples with titanium minerals, which is evidence for highly metallic source magma, as one would expect if the primitive mantle was driving the system.

Many of the textural features of the Coucal Formation can also be explained by a hydrothermal origin. Two samples studied, C17 and C20, contain small iron-oxide spherules that appear to have settled into the iron bands pervading the chert layers. According to Dekov et al., (2003) these spherules could have formed diagenetically, adjacent to oxidized sulfide grains after plume fall-out, or from plume fall-out of oxyhydroxide material [5]. If these spheres formed diagenetically, we would expect to see more compositional variation and a larger size distribution. The fact that the spheres are all nearly 10 m in diameter and have the same iron oxide composition does not support this idea. It is also unlikely that the spheres formed on the sides of oxidized sulfide grains because there are no sulfide or sulfate grains found in those thin sections. These spheres may have formed through eruptions of iron oxide grains at a hydrothermal vent, however, and given the context of the area this is the most likely option.

Another interesting feature found in all of the cherts studied is the relationship between carbon grains and iron oxides. More often than not, carbon grains are surrounded or overgrown with iron oxide (Figs 8 and 9):

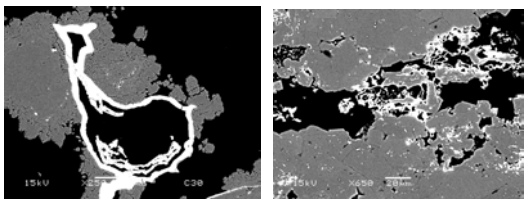

Figs 8 and 9: BSE images from samples C30 and C23 showing the relationship between carbon and iron oxides in these cherts. The black grains are carbon and the white grains are iron oxide.

This strongly suggests an intimate relationship between the carbon and iron oxide, and from this it follows that the carbon is abiotic in origin. There is an abiotic process, Fischer-Tropsch Synthesis, in which the crystal faces of iron oxide and sulfide grains are used as a base to form organic compounds [6]. Iron oxides are very good catalysts for this reaction. Both magnetite and hematite are widely available in a hydrothermal environment. These oxides appear not only in conjunction with carbon grains but also as independent grains which create the bands of iron in the chert. With all of the iron available to a hydrothermal system in the early Archean environment, it is easy to explain the presence of carbon in terms of Fischer-Tropsch Synthesis.

CONCLUSION: The Coucal Formation in northwestern Australia provides a unique opportunity to look into processes working in the Archean environment. Hand specimen analysis, optical and scanning electron microscopy, and whole rock geochemistry suggest that the Coucal Formation formed in a hydrothermal environment. This is not hard to envision given the rapid heat loss and volcanic activity at the start of Earth's history. This scenario fits well within the overall context of the area, given the hydrothermal origin of many of the Archean formations overlying the Coucal Formation (e.g. The Apex chert [2]). Given the surrounding geology, mineral and trace element evidence and textural clues, we conclude that the Coucal Formation is a hydrothermal deposit and the carbon contained therein is abiotic in origin.

REFERENCES: [1] Van Kranendonk, M.J., 2000. Geology of the North Shaw 1:100,000 Sheet. Western Australian Geol. Survey, 1:100,000 Geological Series Explanatory Notes. [2] Brasier, M.D., Green, O.R., Jephcoat, A.P., Kleppe, A.K., Van Kranendonk, M.J., Lindsay, J.F., Steele, A. and Grassineau, N.V., 2002, Questioning the evidence for earth's oldest fossils. Nature, 416, 76-81. [3] Pearce, J. A. and Cann, J. R., 1973, Tectonic setting of basic volcanic rocks determined using trace element analyses. Earth and Planetary Science Letters, 19, 290-300. [4] Peter, J. M. and Scott, S. D., 1988, Mineralogy, composition, and fluid-inclusion microthermometry of seafloor hydrothermal deposits in the southern trough of Guaymas Basin, Gulf of California. Canadian Mineralogist, 26, 567-587. [5] Dekov, V. M., Marchig, V., Rajta, I., and Uzonyi, I., 2003, Fe-Mn micronodules born in the metalliferous sediments of two spreading centres: the East Pacific Rise and Mid-Atlantic Ridge. Marine Geology, 199, 101-121. [6] Lindsay, J.F., Brasier, M.D., McLoughlin, N., Green, O.R., Fogel, M. Steele, A. and S. A. Mertzman, S.A., submitted, The problem of deep carbon–An Archean paradox. Precambrian Research.

Automated Classification of Martian Topographical Data

Brian D. Bue Advisor: T. F. Stepinski

I. Introduction

The Mars Global Surveyor (MGS) spacecraft, equipped with the Mars Orbiter Laser Altimeter (MOLA) instrument, has gathered a wealth of precise topographical data on the surface of Mars. By the time the MOLA instrument ceased mapping in June 2001, it had accumulated over 640 million measurements of the Martian surface and atmosphere [1]. The analysis of this data is essential to understand the fundamental geological processes that have shaped Mars to its present state. A major step in the analysis is the creation of geologic and/or geomorphic maps of the Martian terrain. Traditionally, the creation of such maps has been done by applying the descriptive method to imagery data. A standard mapping technique has been developed [2] to manually identify topographic, stratigraphic, and tectonic relationships and to produce geologic maps. However, accurately describing image data by hand for large geographical regions is a arduous process. Therefore, tools that automate certain aspects of the descriptive method would be beneficial to the field of planetary geomorphology as a whole, and would be particularly beneficial in the study of Martian geomorphology.

Utilizing techniques from the fields of terrestrial hydrology, artificial intelligence, data mining and image processing, we have developed a technique for the fast, automatic classification and statistical analysis of topographical data. This method can help to expedite the process of generating geologic and geomorphic maps.

This paper is structured as follows. In section 2, the concept of a Digital Topography Model (DTM) is introduced. In section 3, we describe the format of the MOLA data to be analyzed. Section 4 briefly explains the two-level classification strategy we employ in clustering the topographical data. The classification results for the Terra Cimmeria site is the subject of section 5, and an extended application of this work to automated crater counting is described in section 6.

II. Digital Topography Models

Our classification technique makes use of the original concept of a Digital Topography Model (DTM) [3]. Derived from the Digital Elevation Model (DEM) concept, a DTM is defined as a quantized planar rectangular space in N dimensions where each $\mathcal{T}$, is assigned a list of N values, $\{\mathcal{T}_1, \ldots, \mathcal{T}_l, \ldots, \mathcal{T}_N\}$, that include, but are not limited to, elevation. The DTM, viewed as a data structure, is a 3-D array consisting of N layers in which each layer contains a 2-D grid of topographical information.

The first layer of the DTM, $\mathcal{T}_1$, contains an elevation field as given by a DEM. The construction of the second layer involves an artificial modification of the original elevation field. This modification is frequently referred to as "flooding." The concept of flood modification originates in terrestrial hydrology when DEM errors created artifact pits in the digital elevation field that needed to be eliminated in order not to interfere with the routing of flow across a DEM. The flooding identifies all enclosed depressions and raises their elevation to the level of the lowest pour point around their edge, thus producing a flooded elevation field. In our approach flooding is not used to correct DEM errors, but instead as a convenient tool to identify terrain depressions and basins. A variable δ representing a difference between flooded and original elevation fields has non-zero values only for pixels located inside depressions. Thus, large values of δ flag pixels located deep inside depressions. In the context of Martian topography, such pixels are likely to be located inside craters. We use variable δ as the second layer ($\mathcal{T}_2$) in the DTM.

Because the elevation field represented by a DEM is quantized it is natural to also quantize the slope directions to only 8 possible values [4]. With such quantization, we calculate the set of eight slopes between a given pixel and it's nearest neighboring pixels using the original elevation field. The pixel's slope is the largest slope in this set. The third layer of the DTM, $\mathcal{T}_3$, holds the values of slopes. Large slopes flag crater rims and other ridges. A different field of slopes is associated with an elevation field modified by the flooding and it constitutes the fourth layer of the DTM, $\mathcal{T}_4$. Pixels with flooded slopes equal to zero are likely to be inside craters. We also store pixels' slope directions, they is not assigned to a layer, but instead used in defining other layers. In flat areas slope directions are assigned using an algorithm developed in [5].

A contributing area is the total number of pixels "draining" through a given pixel. This is another concept that originated in terrestrial hydrology. Here we use the term draining as a metaphor for connectivity between different pixels in a landscape. A pixel counts toward the contributing area of a given pixel if there is a chain of slope directions that links them. Small values of contributing area flag pixels located on topographic peaks, ridges, and divides. Large values of contributing area flag potential channels. Using elevation field modified by flooding leads to different contributing areas. The fifth and sixth layers of the DTM, ($\mathcal{T}_5$ and $\mathcal{T}_6$), hold values of contributing areas calculated on the basis of original and flooded elevation fields, respectively.

The first layer $\mathcal{T}_1$ is essentially the original DEM of the area under investigation. Other layers are calculated using the software suite TARDEM [6]. Note that a value assigned to a pixel in some layers depends on information gathered from a neighborhood (of varying size) of this pixel. This makes pixels "aware" of their topographic context.

III. Data

Our data consists of Martian topography information from the MOLA instrument organized into DEMs. The DEMs are extracted from the MOLA Mission Experiment Gridded Data Record (MEGDR) at a resolution of 128 pixels per degree, which is the highest resolution available to us at this time.

There are several issues that must be considered before processing the data. Namely, edge-contamination, outliers, and normalization.

Edge Contamination: Edge contamination is a phenomenon that occurs when drainage is inwards from region boundaries or areas with no data values for elevation. We solve this issue by lowering the edges of a DEM to the minimum elevation value in the site.

Outliers: Outliers should be very rare in this data set but the data must still be examined as a single outlier can corrupt an entire layer in normalization phase. Standard statistical methods (i.e. Histogram analysis) were used to find and remove any of the initial data values that were considered outliers.

Normalization: Since each layer of the DTM has a different physical meaning, the range of the distributions involved will vary. Currently, we normalize each layer so its values are in the range (0,1). This allows each layer to contribute equal weight in comparing the "distance" between pixels.

B. Bue is with the Departments of Computer Science and Mathematics, Augsburg College, 731 21st ave. N., Minneapolis, MN 55454, USA, now with the Department of Computer Sciences, Purdue University, 250 N. University St., West Lafayette, IN 47907, USA (e-mail: bryn@disambiguate.info)

Dr. T. F. Stepinski is with the Lunar and Planetary Institute, 3600 Bay Area Blvd., Houston, TX 77058, USA (e-mail: tom@lpi.usra.edu)

IV. Pixel Classification in the DTM

After all layers of the DTM are constructed, each pixel (x_0, y_0) holds a vector called a descriptor because it contains information capable of determining the topographical context of a pixel. We employ a two-level approach similar to [7] involving a Self-Organizing map and Ward's minimum variance grouping method to classify the DTM.

The creation of a Self-Organizing map (SOM) is the first step in our pixel classification approach. The SOM is a neural network technique that groups similar vectors into nearby points on a 2-D grid composed of nodes. Through an iterative procedure, the entire set of pixels (a large number, up to 10^8) is mapped into grid's nodes (a small number, of the order of 10^2 -10^3) in such a way that similar pixels are associated with neighboring nodes. Because the number of nodes is much smaller than the number of pixels, many pixels are mapped onto a single node. Thus, each node is represented by a representative pixel, also known as a "codebook vector", an average of all pixels mapped to that node.

The SOM_PAK application developed by Kohonen et al. [8] was used to create the Self-Organizing map of our DTM data. We define a 30x30 rectangular SOM grid with Gaussian neighborhood type. Experimentation with larger grid sizes did not result in noticeably higher quality clusterings. The SOM vectors pass through two "training" phases where the SOM is first organized, then fine-tuned.

The second step in our two-level classification approach is to cluster the SOM codebook vectors with Ward's Minimum Variance grouping method. This agglomerative, hierarchical clustering method seeks to partition data in a manner which minimizes the "information loss" associated with each grouping. At each step in the analysis, the union of every possible cluster pair is considered and the two clusters whose fusion results in the minimum loss of information are combined. Information loss is defined in terms of an Error Sum of Squares criterion, where $ESS = \sum_{i=1}^{n}(x_i)^2 - \frac{1}{n}(\sum_{i=1}^{n} x_i)^2$. We create a dissimilarity matrix of the Euclidean distances between all of the codebook vector pairs. Using the dissimilarity matrix, we cluster the codebook vectors using Ward's method in the statistical computing environment R [10]. The clustering result is used to label the representative pixels in the SOM, which is then used to create a "thematic grid."

V. Application: Terra Cimmeria Region

To demonstrate the capabilities of our method, we classified a fairly large area near the Terra Cimmeria region of Mars. This area was studied thoroughly by Irwin and Howard [11]. The region's coordinate bounds are 124.25^o W, 136^o E, -30.75^o S, and 0^o N and its area is 593 km across at the equator.

The DEM under investigation has 3828 rows, 1391 columns, for a total of 5324748 pixels. After we perform the pre-processing tasks described above, we have the final dimensions of 3824 rows and 1387 columns of classifiable pixels. TARDEM processing takes 17 hours, 19 minutes, 33 seconds. SOM_PAK processing takes 1 hour, 21 minutes, 42 seconds. Other procedures (data conversion, formatting, statistics generation) take approximately 45 minutes. The thematic map for the region derived from the DTM data (Fig. 1) took less than 20 hours to process on a 3GHz Pentium IV machine.

VI. Analysis of Terra Cimmeria Classification

The data from the classification is interpreted by assigning colors that depict the physical meaning of the clusters. We created classifications with 12, 20, and 30 clusters and found that 20 was the best number for this region as it covered the majority of the expected terrain and had very few extraneous clusters (clusters that have near-identical features). Table 1 is a listing of the mean values for each cluster class, which we can use to determine the physical characteristics of each cluster.

To interpret the physical meaning of our clusters, we rely on statistical output data from the classification. In this case, classes 4, 5, 6, 8, and 9 represent the crater classes in this thematic map. Plains are represented by classes 10, 11, 12, 13, 15, and 17, and the ridges consist of classes 14, 16, 18, and 20. Classes 16 and 20, on further investigation were found to be nearly equivalent in physical interpretation, so they were combined into the same class. Finally, class 7 is surely a channel structure due to its high flooded contributing area value.

TABLE I
Mean values of Terra Cimmeria Region classification

class	count	elevation	difference	orig. slope	flood slope	orig. contrib.	flood contrib.
1:	147855	0.138265	0.003250	0.030937	0.021858	0.003462	0.000216
2:	47904	0.111471	0.104112	0.040454	0.000002	0.005315	0.001513
3:	95829	0.317799	0.117415	0.039028	0.017017	0.003530	0.000690
4:	264925	0.661358	0.162938	0.018072	0.000001	0.003545	0.000771
5:	346493	0.684071	0.284778	0.044598	0.000000	0.003787	0.000200
6:	176887	0.580234	0.478165	0.031937	0.000000	0.006218	0.000554
7:	5741	0.614450	0.051613	0.024839	0.002888	0.004587	0.380068
8:	201939	0.716870	0.081926	0.021361	0.000000	0.003586	0.000236
9:	186598	0.746666	0.071662	0.176276	0.003298	0.002048	0.000143
10:	263729	0.499763	0.006120	0.044725	0.034003	0.002505	0.000185
11:	860601	0.672636	0.004904	0.025880	0.018148	0.002297	0.000239
12:	43584	0.199379	0.004587	0.131759	0.102546	0.001549	0.000084
13:	580114	0.793648	0.005109	0.015229	0.006688	0.002573	0.000297
14:	58393	0.302147	0.001168	0.259283	0.247219	0.001432	0.000047
15:	486640	0.738645	0.001654	0.021643	0.016872	0.002946	0.000214
16:	42531	0.545138	0.002825	0.198896	0.174749	0.001345	0.000046
17:	649425	0.846366	0.001636	0.025609	0.022547	0.002038	0.000051
18:	319308	0.821859	0.000000	0.096489	0.093069	0.001013	0.000007
19:	454613	0.772807	0.000000	0.046260	0.044411	0.001316	0.000030
20:	70779	0.794888	0.000000	0.278211	0.249597	0.000747	0.000003

VII. Crater Counting

Using our classification, we can automate the process of crater counting. After a thematic map is generated, in most cases, we will have several clustering results that correspond to impact craters when interpreted physically. Using techniques from integral geometry [12], we can algorithmically identify a significant number of these craters.

The clusters identified as craters are combined to output a binary image in which all objects identified as craters are black, while all other objects are white. Applying the image segmentation algorithm developed by Chang [13], we assign labels to each pixel in each single-connected object. Using methods from integral geometry, we can calculate the Minkowski Functionals (area, perimeter, and Euler numbers) for each object in the binary image.

We can subsequently derive the circularity of each object from the Minkowski Functionals. The circularity of an object is defined by the equation $circularity = \frac{4\pi(area)}{(perimeter^2)}$. Circularity values near unity represent "perfect" circles. Since, statistically speaking, most craters exhibit circular geometrical properties, we can hypothesize that the objects with circularity values near 1.0 are craters.

We have applied our automated crater counting method to the Terra Cimmeria region. Overall, our algorithm has found 2326 crater candidates. Total of 891 of them have diameter $>$ 2 km. For comparison Irwin and Howard have found 890 craters with that size. The near-perfect agreement in the total number of craters is probably coincidental, because our current, preliminary algorithm excludes some true craters and includes some non-craters. Nevertheless, we are confident that with future development our algorithm will reliably count craters. We have found 303 craters with $2 <$ diameter < 3 km, while Irwin and Howard have found 368.

VIII. Conclusion and Discussion

In this paper we have shown that we can automatically classify and characterize MOLA data to generate thematic maps of Martian

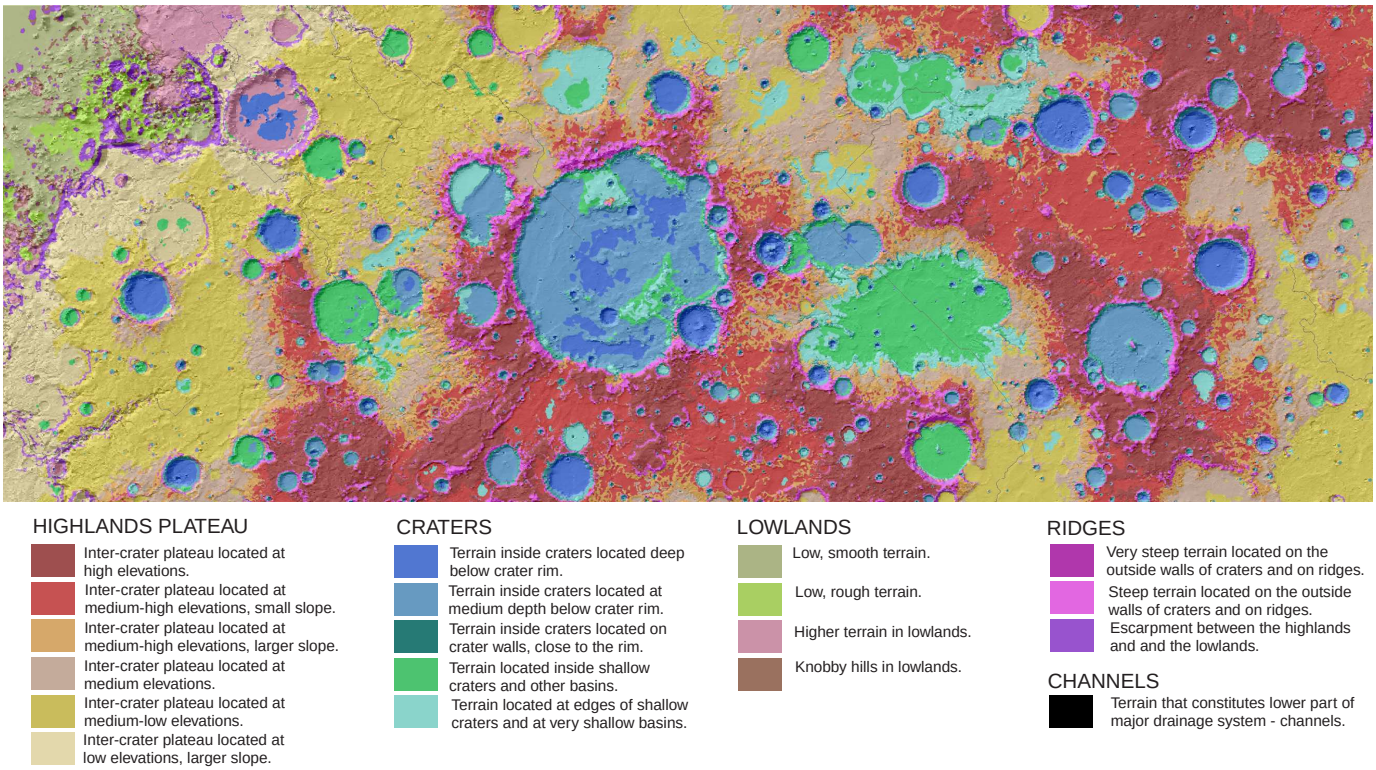

Fig. 1. Thematic Map of Topography for Terra Cimmeria region. Pixels that belong to the same class are indicated by the same color value. The legend below the map describes the physical characteristics of each cluster.

topography. The power of this classification is that it is done at the pixel level, so each pixel in the DTM contains local topographical information.

In order to get a more generalized classification result, we can classify multiple DTMs from differing regions. This was performed on several DTMs of the Margaritifer Sinus region and yielded comparable results to other, individual classifications.

The classification is also very efficient, primarily as a result of the two-level approach to clustering. Thematic maps of topography can be created in a matter of hours for very large regions. The largest DTM classified with this method had dimensions 3021x2063 and took less than 24 hours to process.

It is possible to extend the DTM to include additional layers. Preliminary work is underway analyzing the effects of adding three new layers to the DTM. The first is a measure of regional roughness, the second measures coherence of slope directions, and the last is a measure of hillslope-to-valley length. Adding these layers may result in the extraction of new topographical features unclassified by the 6-layer DTM.

The automated classification and characterization of craters is another significant application of this research. Applying the crater counting algorithm to each individual crater cluster (instead of the combined levels) may result in more accurate counts.

IX. Acknowledgements

I would like to thank Dr. T. Stepinski for his guidance on this project, and everyone at the Lunar and Planetary Institute for inviting me to participate in their internship program.

References

[1] R. Kirk, J-P Muller, and Mark Rosiek. “ISPRS WG IV/9: Extra-terrestrial Mapping”, *Progress Report*, International Society for Photogrammetry and Remote Sensing, 23 Jan. 2003. Accessed 04 Aug. 2004. http://astrogeology.usgs.gov/Projects/ISPRS/INFO/2001report.txt

[2] D. E. Wihelms, “Geologic Mapping”, In *Planetary Mapping*, (R. Greeley and R. Batson, Eds.), Cambridge, UK: Cambridge Univ. Press, pp209-260, 1990. vol.

[3] T. Stepinski and R. Vilalta, “Digital Topography Models for Martian Surfaces”, *IEEE Geoscience and Remote Sensing Letters*, to appear.

[4] J. F. O’Callaghan and D. M. Mark, “The Extraction of Drainage Networks from Digital Elevation Data”, *Computer Vision, Graphics and Image processing*, vol. 28, pp. 328-344, 1984.

[5] J. Garbrecht and L.W. Martz, “The Assignment of Drainage Direction Over Flat Surfaces in Raster Digital Elevation Models”, *Journal of Hydrology*, vol 193, pp. 204-213, 1997.

[6] D. G. Tarboton, R.L. Bras, and I. Rodriguez-Iturbe, “The analysis of river basins and channel networks using digital terrain data”, *Technical Report* no. 326, Ralf M. Parsons Lab., MIT, Cambridge, 1989. http://www.engineering.usu.edu/cee/faculty/dtarb/tardem.html. Accessed 10 Jun. 2004.

[7] J. Vesanto and E. Alhoniemi, “Clustering of the Self-Organizing Map”, *IEEE Transactions on Neural Networks*, vol. 11, no. 3, pp. 586-600, 2000.

[8] T. Kohonen, J. Hynninen, J. Kangas, and J. Laaksonen. “SOM_PAK: The Self-Organizing Map Program Package”, *Technical Report* A31, Helsinki University of Technology, Laboratory of Computer and Information Science, FIN-02150 Espoo, Finland, 1996. Accessed 20 May 2004. http://www.cis.hut.fi/research/papers/som_tr96.ps.Z.

[9] J. H. Ward, Jr., “Hierarchical Grouping to Optimize an Objective Function”, *Journal of the American Statistical Association*, vol. 58, issue 301, pp. 236-244. 1963.

[10] B. D. Ripley, “The R project in Statistical Computing”, *MSOR Connections. The newsletter of the LTSN Maths, Stats & OR Network*, vol. 1, no. 1 pp. 23-25, February 2001.

[11] R. P. Irwin III and A. D. Howard, “Drainage Basin Evolution in Noachian Terra Cimmeria, Mars”, *Journal of Geophysical Research*, vol 107, No. E7 pp. 10-1 - 10-23, 2002.

[12] K. Michielsen and H. De Raedt, “Integral-Geometry Morphological Image Analysis”, *Technical Report* no. 347, Physics Reports, Elsevier Science B.V., 2001.

[13] F. Chang, C-J. Chen, and C-J. Lu, “A Linear-Time Component-Labeling Algorithm Using Contour Tracing Technique”, *Computer Vision and Image Understanding*, vol. 93, no. 2, pp. 206-220, 2004.

Mineralogy and Petrology of Lunar Mare Basalts LAP 02205, LAP 02226, LAP 02224 and LAP 02436.

S.J.Collins[1] K.Righter[2] and A.D.Brandon[2]; [1]Imperial College, London. Email:sarah.collins@imperial.ac.uk
[2]ARES, NASA, Johnson Space Center, Houston

1. Introduction: LAP 02205 is a lunar mare basalt meteorite found in the Lap Paz ice field of Antarctica in 2002 [1]. Three similar meteorites were also found within the same region [1]. These are LAP 02224, LAP 02226 and LAP 02436 (these are LAP meteorites). The LAP meteorites all contain a similar mineral composition, texture and mineral assemblage. The LAP meteorites likely represent an area of the moon, which has never been sampled by Apollo missions, or other lunar meteorites. It is therefore crucial that these meteorites are studied and their origin is understood. The data from this study is compared to some of the Apollo samples in order to constrain their origin.

2. Methods: The LAP meteorites were examined optically using a petrographic microscope before an analysis was undertaken using the Cameca SX100 electron microprobe calibrated with natural and synthetic mineral standards. Modal analyses of the meteorites (Table 1) were determined using X-Ray maps and analyzed using an IDL image-processing programmer. These were used in conjunction with the mineral major element data obtained on the Cameca to determine the bulk compositions of the LAP meteorites (Figure 1). The collected data was subsequently compared to referenced Apollo sample data. Oxygen fugacity was determined using ulvospinel–ilmenite-iron equilibrium and quartz-fayalite-iron equilibrium from O'Neil [2] [3], respectively. RAMAN spectroscopy was used to determine the polymorph of silica contained in the LAP meteorites. Liquidus temperatures of the basalts were calculated using MELTS.

	LAP 02205	LAP 02226	LAP 02224	LAP 02436
Pyroxene	52.1	54.7	50.5	56.4
Plagioclase	36.7	33.5	39.3	32.9
Ilmenite	7.6	6.3	5	6.9
Olivine	2	4	2.2	2.8
Spinel	0.03	0.2	0.6	0.03
Silica	1.6	1	0.8	0.7
Iron metal	tr	tr	tr	tr
Troilite	tr	tr	tr	tr

Table 1: Modal analysis of the LAP meteorites.

3. Texture and Paragenesis: The LAP meteorites all show similar texture and mineralogy. They are all medium to coarse-grained subophitic basalts, with a dominance of pyroxene, plagioclase and ilmenite. Each contains traces of olivine, spinel and metal. Textural comparison of these rocks with other terrestrial and Apollo samples suggest that they are slowly cooled melts which formed at the lunar surface in the middle of a basalt flow anywhere between 2-10 m thick (personal communication – Lofgren.G). From the basalt and olivine morphology it can be inferred that the basalts cooled between 1/10th –1 °C per hour (personal communication – Lofgren.G). The LAP meteorites contain heterogeneous melt veins and pockets whose composition is similar to the bulk composition of the rock with only limited variation (Figure 1). The shock-forming event resulted in partial melts that infiltrated as veins from surrounding regions of each rock. This is inferred due to the minimal shock effects observed in the crystals. There is slight undulatory extinction within plagioclase grains but no more than has been observed in un-shocked terrestrial basalts.

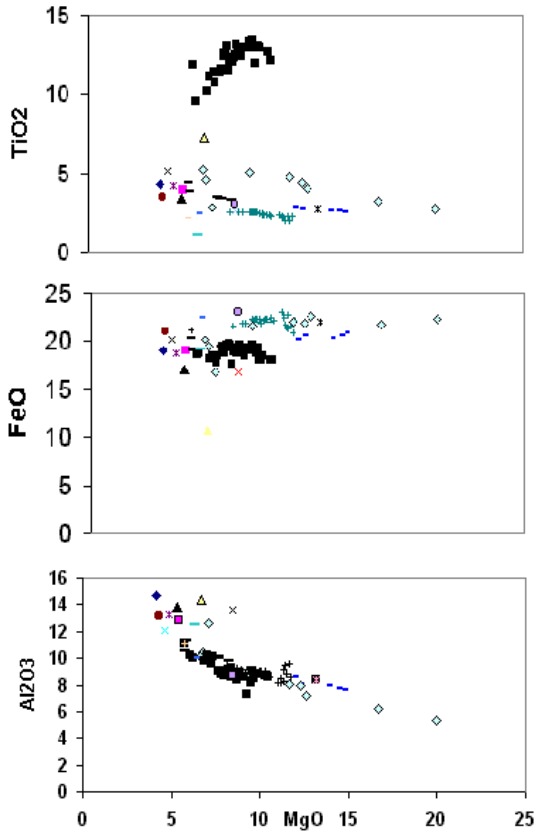

Figure 1: Major element compositions of lunar basalts.

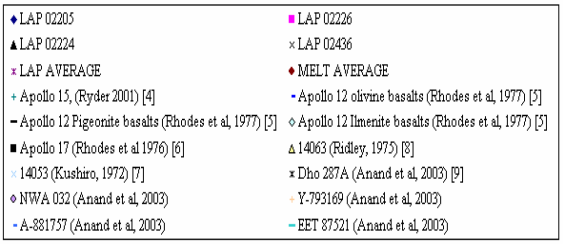

4. Bulk Composition: The major element characteristics of the LAP meteorites display limited variation (Figure 1). The LAP meteorites TiO_2 compositions are similar to the Apollo 12 ilmenite basalts where they plot within the upper range of the low-Ti lunar samples. An interesting result is that the LAP meteorites also show relatively high Al_2O_3 but seem to be depleted in MgO compared to the other lunar samples. High alumina basalts were found in the Apollo 14 samples, 14063 and 14053 [8], [7]. These differ from the LAP meteorites as their ilmenite compositions contain larger amounts of MgO and therefore larger bulk MgO.

4. Mineralogy:

4.1 Olivine: The olivine phenocrysts within the LAP meteorites have a similar habit and grain size. Olivines are generally subhedral in shape although some grains have a skeletal habit with subhedral outlines. The olivine compositions range from Fo_{53} to Fo_{62} is the cores and Fo_{46} to Fo_{57} in the rims, indicative of Mg depletion and Fe enrichment towards the rims of the grains, (Figure 2). The modal proportion of olivine in the four LAP meteorites ranges from 2 to 4% (Table 1).

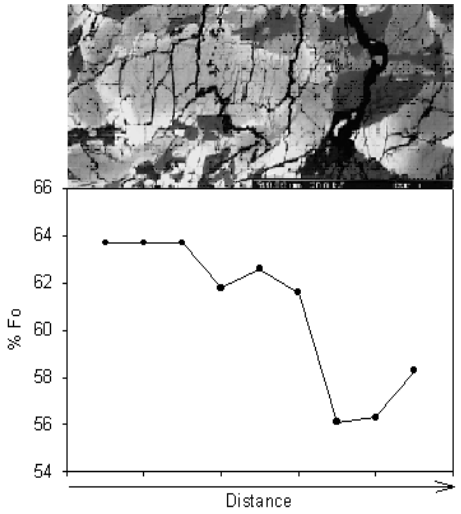

Figure 2: Transect from an olivine phenocryst in LAP 02226, shows the variation in forsterite content from the core to the rim.

4.2 Pyroxene: The pyroxene is either intersertile or enclosing plagioclase within all of the rocks. Pyroxene grains have strong chemical variation from orthopyroxene to pigeonite. The orthopyroxene has strong Fe enrichment and Mg depletion towards the rims of grains and they contain pigeonite cores. Thin augite lamellae are also present within the grains indicative of slow cooling rates. This feature results from subsolidus exsolution of augite and pigeonite.

4.3 Plagioclase: Plagioclase is a dominant component in the LAP meteorites and ranges from 32.9 to 39.3 modal percent (Table 1). It occurs commonly as laths but in some cases has a blocky

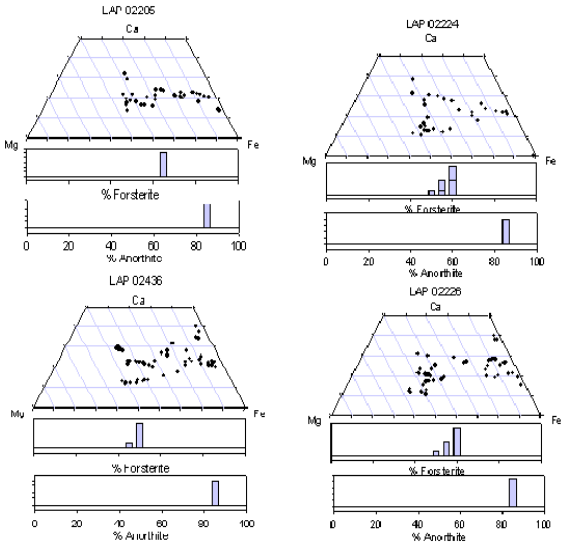

texture. The plagioclase compositions of the LAP meteorites range from An_{85} to An_{89}.

Figure 3: Pyroxene, Olivine and Plagioclase compositions within LAP 02226, LAP 02224, LAP 02436 and LAP 02205, clockwise from left.

4.4. Ilmenite: Ilmenite occurs within the LAP meteorites as the most dominant opaque. The ilmenites are primary minerals that precipitated from the cooling magma as lath like crystals showing some features of a skeletal texture. Modal percent of ilmenite within these meteorites ranges from 5% to 7.6% (Table 1). Ilmenite in these samples are strongly depleted in MgO with a range from 0.02 to 0.24 wt. %. This range in MgO contents are low compared to ilmenite from other lunar basalts, which ranges from 1 – 9 wt. %. These low MgO concentrations in ilmenite result in low MgO contents in the bulk rocks (Figure 1). These low MgO concentrations result in distinct bulk compositions for these meteorites compared to other lunar basalts.

4.5 Baddeleyite: Occurs in association with ulvospinels, ilmenite and troilite.

4.6 Spinel: Spinel in these samples make up 0.03 to 0.6 modal % (Table 1). Ulvospinel occurs as equant grains with little zonation. Small chromite inclusions are present within olivine phenocrysts and are thought to have been the earliest spinels to crystallize [10]. Chromite crystallization was followed by Cr – poor ulvospinel (Figure 4). The V-Cr substitutional trend within the samples shows V preference for other phases at the beginning of crystallization [11]. This suggests that the ulvospinel crystallized later in the sequence than the pyroxene. The Cr/Al ratios show

that the parent liquid was enriched in Cr relative to Al. However the ulvospinels are Cr-poor, again showing that the chromite inclusions within the olivines were an earlier phase than the ulvospinels.

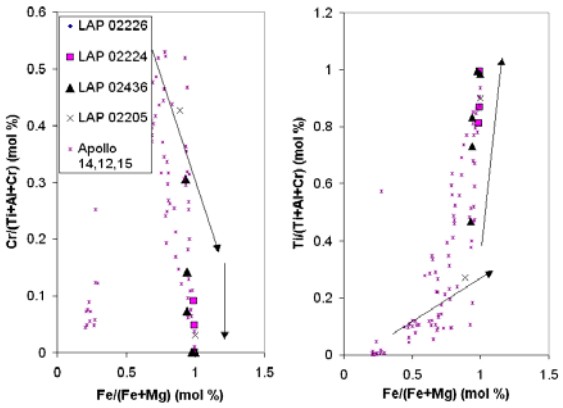

Figure 4: Ulvospinel compositions of all four samples show the early chromium inclusions to the later Cr poor ulvospinels.

4.7 Metal: Metal grains are small (10-20 microns) and are commonly associated with spinel and sulphide within the LAP meteorites. There is a small amount of compositional variation within the metal grains throughout these rocks. This is thought to be due to the limited variation within the bulk composition of the LAP meteorites [12]. The individual grains are homogeneous throughout. The metal grains are dominantly iron with 5.6 to 7.7 wt. % Ni and wt.%. 1.3 to 1.7 Co. Trace amounts of S and no P were detected. It has been suggested that metals which form earlier would be higher in Ni and Co than those associated with spinels which crystallized in the later stages of cooling [12]. In lunar basalts early crystallized metal and troilite have higher Ni and Co than late stage metal [12]. This relationship was also observed within the LAP meteorites. For those grains that crystallized later, troilite had taken up more Ni and therefore the later crystallised metals were more depleted in Ni than the earlier ones.

4.8 Troilite: Troilite is present in trace amounts and with equant morphology. Troilite is typically found in association with oxide grains and in some cases with metal.

4.9 Silica: The LAP meteorites contain cristobalite silica polymorphs. This was determined using Raman Spectroscopy. Cristobalite is found as trace amounts within the samples with 0.7 to 1.6 modal percent. Cristobalite crystallizes at pressures of <1GPa and temperatures between 1450°C and 1700°C. This disagrees with the liquidus temperatures from MELTS calculated to be between 1159°C and 1206°C. It is likely therefore that cristobalite crystallised within the LAP meteorites metastably.

5. Oxygen Fugacity of the Mare Basalts: The fugacity of the LAP meteorites was determined to be -17.2 log10fO_2. The oxidation state of the basalts at the time of crystallization was below the Iron-Wustite buffer by –1 log unit. This oxygen fugacity agrees with fO_2 data from other lunar material [13]. The presence of metallic iron within the samples also supports the conclusion of a strongly reduced lunar mantle below the IW oxygen buffer. The question of whether the reducing conditions originated within the crust and mantle of the moon or during magma evolution is still under speculation [13] but more primitive basalts will be needed for a better understanding.

6. Conclusions: The textures and mineralogy of these four LAP meteorites are similar enough to show that they originated from the same lava flow or group of flows. The LAP meteorites contain high Al_2O_3 but are depleted in MgO compared to other lunar samples, at least in part resulting from the ilmenite compositions. The LAP meteorites originated from the middle of the lava flow between 2 and 10 meters thick which cooled between $1/10^{th}$ –1°c per hour (personal communication – Lofgren .G). The oxidation state of the basalts at the time of crystallization was below the Iron-Wustite buffer by –1 log unit. The liquidus temperatures of the LAP meteorites range from 1159°C and 1206°C. This does not correlate with the presence of cristobalite within the LAP meteorites. Hence, it is inferred that cristobalite occurs metastably within these samples.

7. Acknowledgements: The Author would like to acknowledge the help of Craig Schwandt with his expertise with the EMP, Loan Le with her help with the RAMAN spectroscopy, and Gary Lofgren for his help with the understanding of the basalt textures. This research would not have been possible without the lunar planetary institute providing the internship, or without the help and support of all those in Building 31 of the Johnson Space centre.

8. References: [1] Antarctic meteorite Newsletter 26 (2003) P.17 [2] O'Neil et al (1988) Geochimica et Cosmochimica acta, P. 2065-2072. [3] O'Neil et al (1987) American Mineralogist, p. 67-75. [4] Ryder and Schuraytz, (2001), Journal of geophysics research, vol 106, P 1435-1451. [5] Rhodes et al, (1977), Proc. Lunar sci. conf. 8^{th} pp. 1305-1338 [6] Rhodes et al, (1976), Proc. Lunar.sci.conf.7^{th} P. 1467-1489. [7] Kushiro et al, (1972) Proc. Lunar.sci.conf. 3rd, P. 115-129 [8] Ridley et al (1975) proc, lunar. sci. conf 6th, P. 131-145 [9] Anand et al, (2003) Meteoritics and Planetary Science, Vol 38, P 485-499 [10] Righter et al, Abstract [11] Laul et al, (1973) proc. lunar. sci. conf. 4^{th}, P.1349 [12] Reid et al, (1970), Earth and Planetary science letters 9, P.1-5. [13] Sato et al, (1973) Proc. Lunar.sci.conf.4. P 1061-1079.

Evidence for Extensive Fluvial Erosion Around Olympus Mons: A Multi-Resolution Survey

Selby C. Cull
Hampshire College

Patrick J. McGovern
Lunar and Planetary Institute

Introduction

The Olympus Mons volcano on Mars, the highest mountain in the Solar System, rises over 23 km above its surroundings. Ringed by a basal scarp up to 10 km high, the volcano is surrounded by wide fan-shaped deposits, called aureole lobes, which extend up to 1000 km from its base [1].

Olympus Mons has been well studied in terms of tectonic and volcanic evolution; however, few studies have focused on fluvial features around Olympus Mons and their relationship to the tectonic evolution of the volcano. Previous studies have examined the small-scale relationship between tectonic and fluvial features around Olympus Mons [2], small-scale fluvial features in and around the aureoles [3, 4], the relationship between volcanics and the cryosphere [5], and the proposed rock glacier deposits on the western flank of the volcano [6, 7]. This study surveys the aureole lobes and regions surrounding Olympus Mons for signs of large- and small-scale fluvial activity.

Data & Methods

This survey used several types of data at different resolutions. First, daytime infrared images from the Thermal Emission Imaging System (THEMIS) aboard *Mars Odyssey* were mosaicked over the region 7 – 34 N and 209 - 236 E using the USGS Integrated Software for Imagers and Spectrometers (ISIS). These images are moderately high-resolution, at 100 meters-per-pixel, and provide nearly complete coverage of the Olympus Mons area. Second, visual THEMIS (THEMIS-VIS) images in the 7 – 34 N and 209 – 236 E range were examined. Though they provide very limited coverage, the THEMIS-VIS images are higher resolution, at about 18 meters-per-pixel. Third, topography data from the Mars Orbiting Laser Altimeter (MOLA) aboard *Mars Global Surveyor* were used (resolution of 1/128th degree per pixel) [8]. Fourth, pulse width data from MOLA (resolution of 1/8th degree per pixel) were used to estimate and compare surface roughnesses. [9]

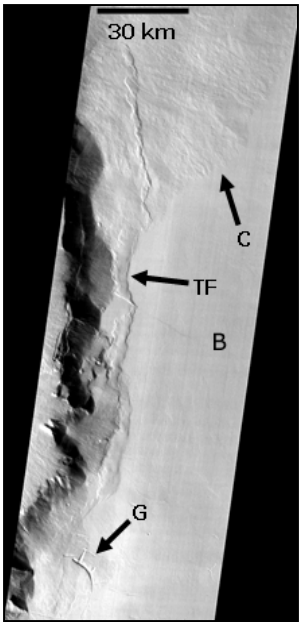

Figure 1 (left): Portion of Mosaic of THEMIS Day IR images I01028005 and I01390005. The western half of the basin (B) is shown. The contact (C) between the lava flows and the overlying sediments is labeled, and is clearly visible in THEMIS Vis image V01028006. The thrust fault (TF) is labeled, and is clearly visible in THEMIS Vis image V06583017. An arcuate graben (G) previously identified by [2] is also labeled. The center of this mosaic is at approximately 17.6 N, 231.5 E.

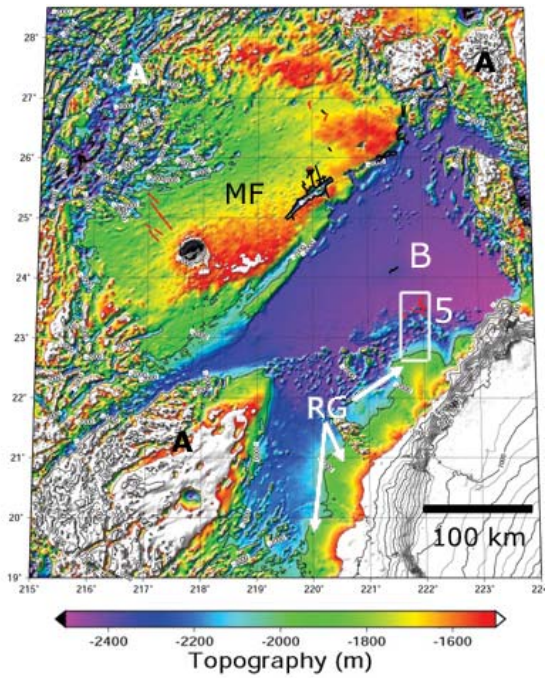

Figure 2 (above): MOLA topographic map of the northwestern basin (B). MF represents a portion of the Medusa Fossae unit mapped by [10], RG shows the location of rock glacier deposits identified by [6, 7], and A represents aureole deposits. The area covered by Figure 5 boxed and labeled.

Results

Evidence for Ponded Water: Two areas around Olympus Mons show evidence of past ponded water (enclosed basin, topographic low, extremely smooth, sediments overlying other features): a small basin near the eastern basal scarp, and a larger area to the northwest of the volcano.

The eastern basin (centered at ~17.6 N, ~231.3 E) is about 60 km wide, 160 km long, and 500 m deep. It is topographically enclosed, and

has an RMS roughness that ranges from 0.7 to 1.0 m in MOLA pulse width data, significantly smoother than its surroundings, which average between 4 and 10 m. The basin is located just east of the basal scarp, and appears to be filled with sediments, which cover lava flows from the edifice (Figure 1 C). A wrinkle ridge cuts these lava flows and traces the western side of the basin (Figure 1 TF).

The northwestern basin (centered at ~24.5 N, ~221.5 E) is much larger: nearly 300 km across, 200 km long, and 500 m deep. It too is topographically low and enclosed (Figure 2), and has a roughness that ranges from 0.7 to 1.0 based on MOLA pulse width data, compared to a roughness between 5 and 15 m for its surroundings. No lava flows were observed within the basin. The unusual smoothness, flatness, low elevation, and lack of lava flows in the middle of a region made of rough, high elevation aureole blocks and lava flows all suggest that this basin also once held ponded water [11].

Evidence for a Relationship Between Channels and Tectonic Features: Previous authors have suggested a relationship between tectonic features and fluvial activity near Olympus Mons [2]. The THEMIS IR and VIS data examined in this survey provide further evidence for such a relationship. Of the 110 tectonic features (faults, wrinkle ridges, graben, etc.) examined in this survey, 79 were associated with or modified by fluvial activity (Figure 3).

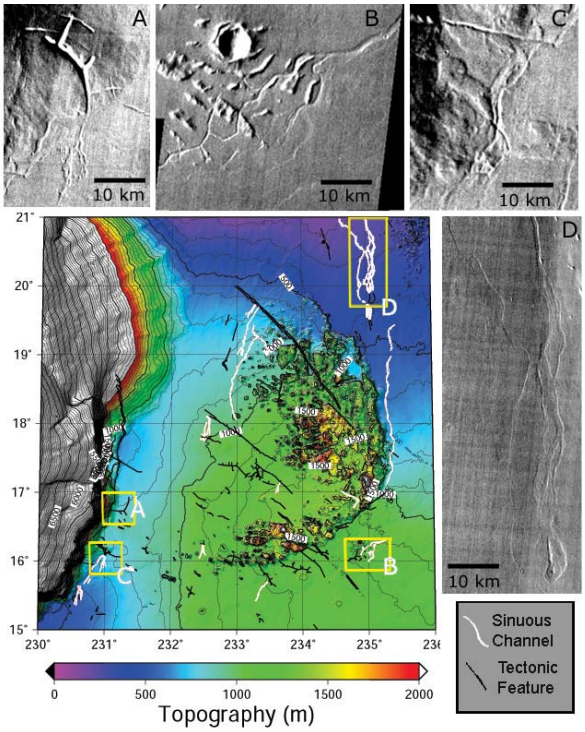

Figure 3 (above): MOLA topographic map of the eastern aureole lobe (bottom left), with tectonic features marked in black and fluvial features marked in red. Some interesting features from THEMIS Day IR mosaics: (A) an arcuate graben (also in Figure 1 G) identified by [2] with distinct channels issuing from it. (B) A network of graben ends as a channel system issues from it. (C) Several sinuous channels issue from a linear graben. (D) Several sinuous channels issue from a collapse pit.

Evidence for a "Spillway": Between the northeast aureole lobe and the Tharsis rise is a narrow, flat plain filled with lava flows. This plain runs continuously for several hundred km, up to the northern edge of the North aureole lobe.

Several THEMIS-VIS images (v05834011, v02139009, v05909003, v08518015, v01490006, v02988003, v02314010) show that this plain is covered with scoured surfaces (Figure 4 B), wide and shallow channels (Figure 4 A, C, D), and stream-lined islands (Figure 4 C, D).

Discussion

This survey found evidence for extensive fluvial activity around Olympus Mons and its aureole deposits. Here we discuss where the water may have come from, where it went, and how it may relate to the tectonics around Olympus Mons.

For the northwestern basin, fluids may have come from a variety of sources. Water has been expelled from the aureole lobes along their margins [3], so water from the northern lobe may have ponded in the northwestern basin. Water may also have come from melting of the nearby glaciers [6, 7]. Although these workers proposed that these glaciers were cold-based, this survey found THEMIS Day IR images showing several channels near these deposits that may be related to basal melting (Figure 5).

For the eastern basin, we interpret the wrinkle ridge running along the basin's edge as a thrust fault indicative of volcanic spreading (e.g., [12]). Further, we propose that water squeezed out along a pressurized detachment from a water-rich layer below Olympus Mons [4] then ponded in the eastern basin, depositing the smooth sediments that now cover the lava flows off the edifice. Since it is a topographic low in the area, the basin may also have been filled by run-off from the surroundings; however, no channels running into the basin were observed. We hypothesize that a similar process of water moving along a pressurized detachment fault from below Olympus Mons may have supplied the water needed to form the glaciers on the western side of the volcano. The fault, though not observed, may be hidden beneath the glacier deposits. The channels observed near the deposits may therefore have come from basal melting or from water moving along the fault.

Further evidence for a water-rich layer beneath Olympus Mons comes from the relationship of tectonic and fluvial features seen around the volcano. Faults are well-known as zones that can facilitate the transport of fluids, and we propose that faults and grabens around Olympus Mons serve as conduits for liquid water to reach the surface [2]. This survey has provided further evidence for a groundwater system beneath Olympus Mons, and

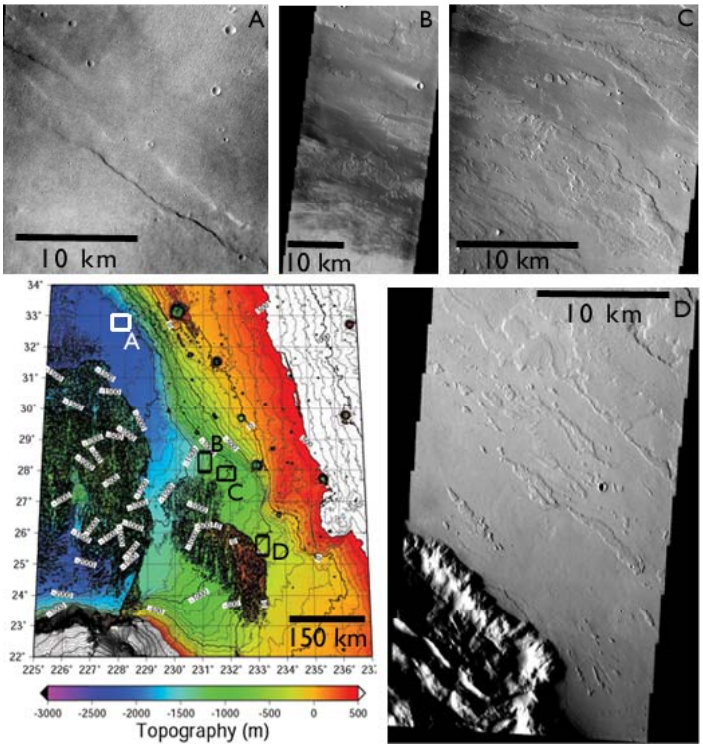

Figure 4 (right): MOLA topographic map of the northeastern aureole lobe (bottom left). The spillway runs from the lower right to upper left, above the northeastern and northern lobes. Some interesting features from THEMIS Vis images: (A) a graben modified by water (uneven banks, flat bottom, branching to the north) from V02988003. (B) Scoured surface from V02164008. (C) Flat, broad channel carved in lava flows with stream-lined islands from V02139009. (D) Flat, broad channel carved in lava flows with stream-lined islands from V05833011.

suggests that it is extensive, extending at least below the southeastern, eastern, and northeastern aureole lobes.

Water issuing from the groundwater system through tectonic features may have joined water running down off the Tharsis rise (e.g., [2]) to produce the features seen in the spillway. The scouring and wide, flat channels observed in the spillway suggest that the flows were rapid, and the absence of deep narrow channels and incomplete stream-lining of islands suggest that the flows were short-lived.

Conclusions

This survey supports the hypothesis that there is a groundwater system beneath Olympus Mons, that this system is extensive, and that its interaction with tectonism has produced much of the fluvial activity observed around the volcano.

We have also identified two potential paleolakes, and a spillway channeling fast and short-lived hydrous flows from the Tharsis rise and eastern/northeastern Olympus Mons aureole deposits toward the northern lowlands.

Future Work

This survey began with THEMIS Day IR images, THEMIS-VIS images, and MOLA topography and pulse width data. The next step will be to expand it to include THEMIS Night IR images, THEMIS temperature data, and Mars Orbiter Camera (MOC) images. The THEMIS Night IR images and temperature data will provide us with thermal inertia information on the sediments filling the two paleolakes, and the MOC images will provide a high-resolution view of select areas in and around the two basins and the spillway. The MOC images will be combined with MOLA data and THEMIS Day IR and VIS images to further characterize the relationship between tectonic features and fluvial activity around Olympus Mons.

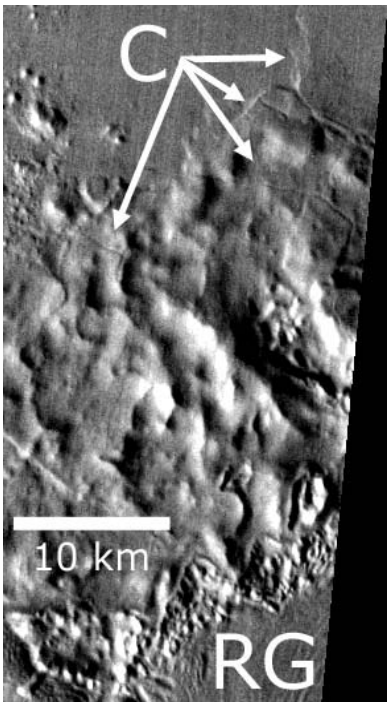

Figure 5 (right): Portion of THEMIS Day IR mosaic showing a corner of the rock glacier deposits (RG) [6, 7] and several sinuous channels (C) running from the deposits into the smooth, flat northwestern basin. The rock glacier deposit continues up along the right side of the image, however, the crucial THEMIS Day IR image that would definitively link these channels to the deposits is missing. Further imaging is needed.

References

[1] Mouginis-Mark PJ et al. (1992) in *Mars* [ed. Kieffer et al.].
[2] Mouginis-Mark PJ (1990) Icarus 84: 362-272
[3] Chittenden D and McGovern PJ (2004) Proc. of Lunar and Planetary Science Conference XXXV, Abstract #2074.
[4] McGovern PJ et al. [2004] JGR *in press*.
[5] Wilson L and Mouginis-Mark PJ (2003) Icarus 165: 242-252.
[6] Milkovich SM and Head JW (2003) Sixth International Conference on Mars, Abstract #3149.
[7] Head JW et al. (2003) Third Mars Polar Science Conference, Abstract #8105.
[8] Smith et al. (2001) JGR 106: 23689-23722.
[9] Neumann et al. (2003) GRL 30: 15-1.
[10] Morris EM and Tanaka KL (1994) USGS Map I-2327.
[11] Morgan J, personal communication, June 2004
[12] Borgia A et al. (1990) JGR 95: 14357-14382.

EXPERIMENTAL PETROLOGY OF THE NEW MARTIAN METEORITE YAMATO 980459. Heather Dalton[1], Donald Musselwhite[2], and Allan Treiman[2]; [1]Department of Geology, Stephen F. Austin State University, Nacogdoches, TX 75962, [2]Lunar and Planetary Institute, 3600 Bay Area Blvd., Houston, TX 77058.

Introduction: Yamato 980459 (Y98) was found in 1998 by a Japanese expedition to the Yamato area of the Antarctic Ice Sheet. It was announced in 2003 as a new Martian meteorite. Y98 is an olivine-phyric basaltic shergottite [1]. The meteorite is composed of 48% pyroxene, 26% olivine, 25% mesostasis, and 1% other minerals. Unlike the other Martian basalts, it contains no plagioclase. The olivines in Yamato 980459 are the most magnesian of all Martian meteorites, and therefore it is believed to be the most primitive [2]. As such, its composition may be the closest to a primary or direct melt of the Martian mantle. The goals of this project were to look for the liquidus at various pressures, and also to look for multiple saturation on the liquidus to discover the environment of the Martian mantle when the meteorite was formed.

Oxide	Y 980459 [3]	Y 980459 [4]	Target Comp	Comp as Weighed	Exp Glass Comp
SiO2	49.40	48.70	49.05	49.24	50.20
TiO_2	0.48	0.54	0.51	0.51	0.50
Al_2O_3	6.00	5.27	5.64	5.67	5.50
Cr_2O_3	0.71	0.71	0.71	0.71	0.66
FeO	15.80	17.32	16.56	16.63	15.82
MnO	0.43	0.52	0.48	0.48	0.49
MgO	18.10	19.64	18.87	18.95	19.35
NiO	0.03	0.03	0.03	0.03	0.01
CaO	7.20	6.37	6.79	6.81	6.97
Na_2O	0.80	0.48	0.64	0.64	1.09
K_2O	0.02	0.02	0.02	0.02	0.05
P_2O_5	0.31	0.29	0.30	0.30	0.36
S	0.07			0.00	0.01
FeS	0.19	0.26	0.23	0.23	
Total	99.54	100.15	99.81	100.00	101.00

Table 1- Pressure experiment starting material. The second and third columns are published compositions of Yamato 980459 from Greshake [3] and Misawa [4] respectively. The target composition is an average of the second and third column. The composition as weighed column is the weight corrected back to the original compounds (FeO, MnO, CaO, Na_2O, K_2O, and P_2O_5) after using Fe_2O_3, MnO_2, $CaCO_3$, Na_2CO_3, K_2CO_3, and $Ca_5(PO_4)_3OH$ to make the sample, and normalized to 100%. The last column is the composition of the pressure experiment Yam 12-4, which produced only glass.

Experimental Procedure: Using the piston cylinder apparatus from Depths of the Earth Company, experiments were conducted at 5, 8, 12, and 16 kbars, at temperatures ranging from 1380°C to 1625°C. The assemblies (Figure 1) consist of a $BaCO_3$ salt cell, a graphite furnace, MgO bushing, an Al_2O_3 disk, and a graphite sample capsule containing the powder of the composition of the Y98 (Table 1). The starting material powders were added as oxides or carbonates and ground together using a mortar and agate pestle. Then the powder was melted completely in a muffle furnace and reground to ensure good homogeneity. The powder was pre-reduced using a vertical furnace at a range of -14.74 to -14.97 log(fO_2). This set the Fe^{2+}/Fe^{3+} ratio between 1.133 and 1.016 [5, 6], which put the oxygen fugacity (fO_2) at IW (iron-wuestite) + 0.6 to 0.8 log units [7]. Graphite sample capsules are used because they control oxygen fugacity. The C to CO reaction maintains the fO_2 at IW + 0.6 to 0.8. In addition, the graphite capsules do not react with the melt (except by the aforementioned fO_2 control), as evidenced by the fact that the composition of the 100% melt runs is essentially the same as the starting material.

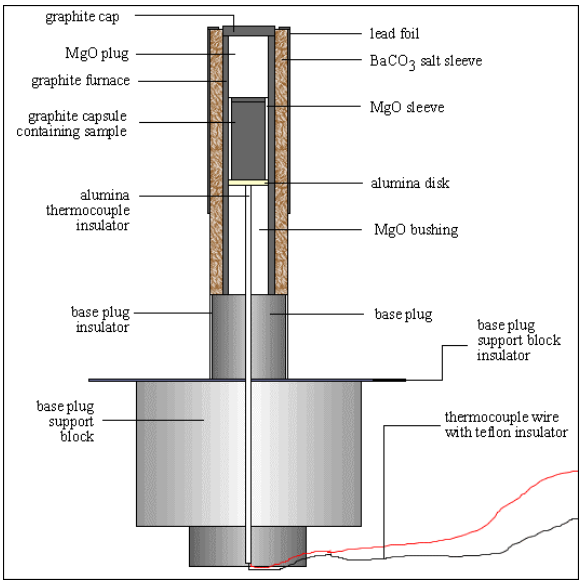

Figure 1- Diagram of piston-cylinder assembly.

The assembly is placed into the piston-cylinder and brought up to 10% above the run pressure. The experiment is then ramped up to run temperature over one half hour. When it has reached run temperature, the pressure is brought down to run pressure. This "hot piston out" method is used to eliminate the friction correction at pressure. The runs ranged from 4 to 24 hours in duration. The runs were then quenched isobarically. Run conditions and run products of these experiments are shown in Table 2 below. In addition to the high-pressure experiments

using the piston-cylinder, we performed two 1-atmosphere experiments using a vertical furnace to make a bead of glass from the starting material. These experiments were run at fO_2 of IW + 0.6 to 0.8.

Table 2 – Run conditions and run products. Problematic runs are italicized.

Sample	Pressure (kbar)	Temp (°C)	Duration (hours)	Results
Yam 2	0	1455	2	glass + quench crystals
Yam 5-2	5	1450	18	olivine + glass
Yam 5-5	*5*	*1500*	*4*	*few olivines + glass*
Yam 5-7	*5*	*1530*	*21*	*olivine + pyroxene + glass*
Yam 12-1	*12*	*1380*	*18*	*olivine + glass*
Yam 12-4	*12*	*1520*	*6*	*glass - t-couple slip*
Yam 12-6	12	1500	6	glass + olivine + pyroxene
Yam 12-12	12	1580	18	few olivines + glass
Yam 12-17	12	1550	24	olivine + glass
Yam 16-18	16	1625	6	glass
Yam 8-19	8	1520	18	glass
Yam 8-20	8	1490	22	olivine + glass
Yam 8-21	8	1450	22	glass + olivine + pyroxene

After a piston-cylinder run, samples were analyzed using the Cameca SX-100 electron microprobe. Atomic weight percentage, compound weight percentage, and visual data were obtained from the microprobe. This allowed us to see at what pressures and temperatures olivines and pyroxenes formed, and also if an error in the experiment had occurred.

Results: Figure 2 on the following page shows the calculated liquidus, experimental liquidus, and the experimental pyroxene-in lines of Yamato 980459. Some experiments were not selected for use in this plot because of atypical results caused by one of two factors: thermocouple slip/misplacement of sample or contamination. Two of the 5kbar runs had abnormally high Al_2O_3 concentrations. It was deduced that the crushed alumina that is used to pack the MgO plug on top of the sample capsule had somehow leaked into the capsule, giving us results that were not typical of the other experiments. In two of the 12kbar runs, the thermocouple slipped, or the sample capsule was not in the hot spot. Yam 12-1 had only a few olivine crystals when it was below the pyroxene line and should have contained a multitude of both olivine and pyroxene crystals. Yam 12-4 was completely glass with no crystals, when it should have been well below the liquidus. However, even the unsuccessful experiments were useful. Figure 3 on the following page illustrates the Fe partitioning between olivine and liquid [8] in the Yamato 980459 high-pressure experiments using data obtained from the electron microprobe. For the most part, the points from the experiments lie near the correlation line from [8], which shows that there is equilibrium partitioning between Fe and Mg in the samples. Table 3 below shows the composition of the results of the high-pressure experiments.

Table 3- Compositions of high-pressure experiments.

Sample	Na_2O	Al_2O_3	CaO	TiO_2	MnO	SiO_2	Cr_2O_3	FeO	MgO	K_2O	Total
OLIVINE											
Yam 5-2	0.01	0.03	0.22	0.01	0.44	37.97	0.48	16.32	43.82	0.00	99.38
Yam 5-5	0.01	0.04	0.21	0.01	0.34	38.67	0.42	13.35	45.66	0.00	98.82
Yam 5-7	0.02	0.14	0.34	0.01	0.46	38.20	0.49	18.68	40.51	0.00	98.91
Yam 8-20	0.02	0.04	0.23	0.01	0.38	39.60	0.43	15.57	43.78	0.00	100.11
Yam 8-21	0.02	0.08	0.28	0.01	0.42	39.23	0.47	17.85	41.32	0.00	99.79
Yam 12-1	0.03	0.08	0.36	0.02	0.50	36.02	0.16	26.49	32.83	0.00	96.78
Yam 12-	0.02	0.11	0.33	0.01	0.44	35.45	0.37	19.06	39.40	0.00	95.88
Yam 12-12	0.02	14.76	0.03	0.44	0.28	1.02	51.74	11.82	16.63	0.00	96.77
Yam 12-17	0.02	0.04	0.26	0.01	0.38	38.88	0.39	14.63	44.68	0.00	99.32
PYROXENE											
Yam 5-7	0.05	1.05	2.07	0.07	0.45	53.28	0.92	12.07	28.14	0.00	98.15
Yam 8-21	0.06	0.64	1.53	0.06	0.40	55.65	0.77	11.12	29.37	0.01	99.65
Yam 12-6	0.08	2.16	2.07	0.09	0.40	54.21	1.16	11.52	28.32	0.00	100.16
GLASS											
Yam 5-2	0.98	6.27	7.68	0.57	0.49	48.54	0.69	15.47	15.16	0.03	96.31
Yam 5-5	1.15	9.29	6.86	0.45	0.46	45.79	0.66	14.40	17.52	0.02	96.99
Yam 5-7	1.04	10.06	9.07	0.60	0.48	49.66	0.63	15.09	12.25	0.04	99.43
Yam 8-19	0.80	5.33	6.57	0.49	0.45	48.31	0.68	15.86	18.48	0.02	97.36
Yam 8-20	1.04	6.12	7.32	0.48	0.47	47.44	0.62	15.87	14.51	0.03	94.61
Yam 8-21	1.09	6.49	8.23	0.61	0.50	49.56	0.69	17.28	14.38	0.03	99.30
Yam 12-	0.29	4.20	6.59	0.26	0.50	48.28	0.69	15.52	20.09	0.00	96.62
Yam 12-4	1.09	5.50	6.97	0.49	0.49	50.20	0.66	15.82	19.35	0.05	101.01
Yam 12-6	1.15	5.71	8.07	0.57	0.48	39.82	0.53	16.58	14.07	0.03	87.42
Yam 12-17	1.16	5.26	7.20	0.44	0.49	44.74	0.59	14.93	14.94	0.02	90.17

In contrast to [2], the Mg numbers of these experiments ranged from 0.79 to 0.86 for olivine and 0.81 to 0.82 for pyroxene. These are lower than the MELTS compositions cited by [2], which have Mg numbers of 86 for the most magnesian foresterite and 84 for the most magnesian enstatite.

The successful experiments showed that the experimental liquidus lies well below the calculated liquidus from the MELTS software, which is illustrated in Figure 2. In addition, MELTS determined the liquidus to be a linear relationship

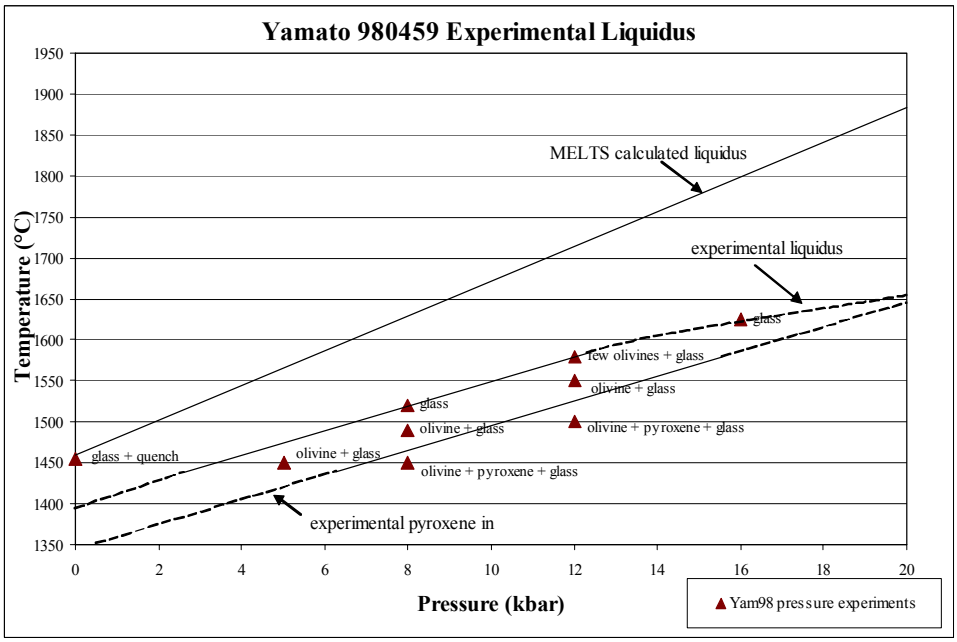

Figure 2- Plot of calculated and experimental liquidus of Yamato 980459. The experimental liquidus line lies well below the calculated liquidus from the MELTS software. Experiments above the experimental liquidus line produced only glass; those between the liquidus and pyroxene lines produced olivine + glass; and those under the pyroxene-in line produced olivine + pyroxene + glass. MELTS predicted pyroxene-in to occur at 1360°C at 1 atmosphere (0 kbar) [2], which is where we predict it to be based on our experimental data.

between temperature and pressure, but experiments show that the liquidus line begins to curve downward slightly as the pressure increases.

Figure 3- Fe partitioning between olivine and liquid. The points are average composition from high-pressure runs, while the line is from Jones [8]. D is the concentration of the crystal/concentration of the melt.

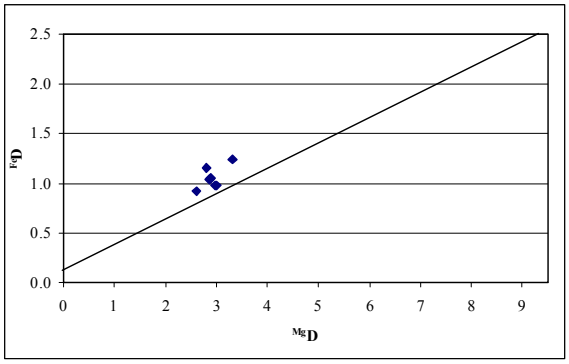

If the liquidus and pyroxene-in lines converge, it would indicate there is a multiple saturation for this composition. Our failure to create a cosaturation could mean several things:
(1) Yamato 980459 is a cumulite with excess olivine;
(2) Y98 left mantle olivine and pyroxene behind at pressures greater than 12 kbar, which corresponds to a depth of 99 km on Mars [9];
(3) Y98 left only olivine behind in its mantle because of prior melting. Further experiments are needed at higher pressures to determine if the liquidus and the pyroxene-in lines converge at higher pressures.

Acknowledgments: I would like to thank Don Musselwhite and Allan Treiman for their encouragement, guidance, and patience throughout the last 10 weeks, and for making my first experience with planetary science one I will never forget. Also I extend thanks to the following individuals: Loan Le for her help in the lab; Craig Schwandt for his time and effort with the electron microprobe; the staff of LPI and JSC; and Kevin Righter, Alan Brandon, and Lisa Danielson for their wisdom, insight, and humor. Without their help, this project would not have been possible.

References: [1] McKay G. et al. (2004) *Lunar Planet. Sci. XXXV* abs. #2154. [2] Koizumi E. et al. (2004) *Lunar Planet. Sci. XXXV* abs. #1494. [3] Greshake A. (2004) *Geochim. Cosmochim. Acta* **68**, 2359-2377. [4] Misawa K. (2003) International Symposium abs. *Evolution of Solar System: A New Perspective from Antarctic Meteorites*, 84-85. [5] Kress V. C. and Carmichael I. S. E. (1988) *Am. Mineral* **73**, 1267-1274. [6] Kilinc A. et al. (1983) *Contrib. Mineral. Petrol.* **83**, 136-140. [7] Holloway J. R. et al. (1992) *Eur. J. Mineral* **4**, 105-114. [8] Jones J. H. (1995) AGU Reference Shelf 3, 73-104. [9] Kiefer W. S. (2003) *Meteorit. Planet. Sci.* **38**, 1815-1832.

FIELD EXPERIENCE FOR MARS EXPLORATION VIA INFRARED SPECTROMETERS. N.G. Heavens, Department of the Geophysical Sciences, University of Chicago, 5734 S. Ellis Ave., Chicago, IL, 60637 (heavens@uchicago.edu). Adviser: L.E. Kirkland, LPI, (kirkland@lpi.usra.edu).

Introduction: The Mars Exploration Rovers (MERs) have completed their primary missions but continue to investigate the Martian surface and atmosphere with the thermal infrared spectrometer Mini-TES. Mini-TES is capable of investigating geologic materials at significant distances from the Rovers. Accurate analysis of these measurements would provide detailed information about the local geologic setting of the Rovers that cannot be provided by the rock-specific APXS and Mössbauer instruments.

Of greatest importance to NASA's Mars Exploration Strategy is the possibility that Mini-TES might detect minerals that form in the presence of liquid water, such as the sulfate mineral jarosite, (K, Na, $H_3O)Fe_3(SO_4)_2(OH)_6$, which has been proposed to be present on Meridiani Planum based on Mössbauer spectroscopy [1]. Here, we analyze Mini-TES-like field measurements of sulfate-rich mining areas in Arizona and Nevada without ground truth (i.e. without direct physical examination of measured sites as would be the case for Mars). We test the identifiability of jarosite and other rocks and minerals in field measurements, investigate sources of error in the mineral abundance mapping techniques used for Mars, and build the framework for a ground truth study that will test the results of this study and thus provide insight into how Mini-TES data can be interpreted more accurately.

Data: During July of 2004, field measurements were made at several operational and closed base and precious metal mining areas in Nevada and Arizona using a Model 100 (M100) Block Engineering Fourier transform interferometer in a raster-scanning configuration. Mini-TES is a raster scanner, and the M100 is the only thermal infrared hyperspectral raster scanner used for Mars analog studies. It measures with the highest fidelity to Mini-TES of any field instrumentation available [2]. Measurements were made at four locations: the Alunite Mining District in Clark County, NV; Yellow Pine Mine in Clark County, NV; Mineral Park in Mohave County, AZ; and Antler Mine in Mohave County, AZ.

Procedure: The field measurements were processed and corrected for atmospheric downwelling radiance using standard methods, including the special ratio correction for the solid phase, then output as separate bands at a resolution of approximately 4 cm^{-1}. The set of these images is known as a "scene" and each pixel in the set of images is called a "pixel." Using the computer application ENVI, it is possible to view the total measured spectrum at each pixel and perform mathematical operations on one or more bands.

To simulate the Pancam instrument on the MERs, photographs were taken at each site measured by the infrared spectrometer. The physical characteristics of geologic materials in the scene such as surface roughness, coatings, grain size variations, reflectance, and visible crystals were inferred from the photographs. Then each scene was examined carefully, pixel by pixel, to identify spectra with the clearest reststrahlen bands, which we call "type spectra." An unstated assumption of many spectroscopy studies is that these type spectra indicate high abundances of a particular geologic material, though it is sometimes admitted that the physical properties of a material more than its abundance control the band strength and contrast of its spectral signature [3] [4]. In addition, many spectra in these scenes often appeared to be mixtures of type spectra. Then using both published [5] and our own libraries of laboratory spectra, a preliminary identification of the material indicated by the type spectrum was made.

Conventionally, the abundances of minerals in a particular scene are mapped to draw connections between the visual appearance of the material and its possible composition, often using a technique called linear mixture modeling. However, linear mixture modeling is extremely sensitive to model inputs, can give absolutely contradictory results, and often makes fits based on spectral features that are insignificant or are due to contaminants. Hence, we wanted to map where in a scene we could actually identify a particular geologic material in the measured spectrum by quantifying the features that are qualitatively indicative of a material.

Therefore, a simplified band parameterization technique [6] was used. The spectral features of each scene were mapped by defining the "strength" of each unique (i.e. no strong band at that wavelength was present in any other spectrum) trough in the type spectrum as 1-T (i.e. the value relative to the theoretical continuum), where T is the minimum emissivity of the trough and the strength of each peak as $P-((T_1+T_2)/2)$, where P is the maximum emissivity value of the peak and T_1, T_2 are the minimum emissivity values of the nearest one (or two) troughs. The strengths of unique reststrahlen bands were summed for each scene and normalized by dividing the band strength value at each pixel by the band strength value at the type spectrum. Multiplying by 100%, a "confidence value" was calculated at each pixel in the scene. This confidence value represents the confidence that a certain spectral signature is present at that pixel. The type spectrum is set arbitrarily at 100% confidence. These "confidence maps," which are analogous to abundance maps, were made for each scene and compared with the photographs.

One drawback of this technique was that the unique bands were often not strong enough to justify the identification of a material, so non-unique bands were used in the mapping algorithm, which could lead to confusion between minerals. Interpretation problems, however, were avoided by mapping confidences for different materials on the same map in different colors to see where mineral mixtures could be present and by viewing the measured spectra of the pixels with the highest confidence values to see if they contained the indicated signature.

Results and Analysis: *Jarosite:* Jarosite is an alkali iron sulfate hydroxide mineral that forms in acidic environments such as weathered ore bodies or acidic hypersaline lakes [7] [8], and mines that use sulfuric acid leaching (e.g., Mineral Park and Antler Mines). Its presence on Mars may indicate that water-rich, acidic environments existed on Mars in the past [9]. In our study, jarosite may have been identified spectrally at both Mineral Park and Antler sites in yellow and reddish-brown fine-grained material and to a lesser extent in pebble to boulder-sized material of the same color. Jarositic signatures were notably absent from apparently self-compacted grey fine-grained material that may have contained material of larger sizes. In most

cases, thermal infrared jarosite signatures from yellow and reddish-brown material were nearly indistinguishable.

What makes these identifications difficult is that the two available laboratory spectra for coarse jarosite differ in band strength and shape. The library spectrum with the weaker bands may have broad bands because it was mixed with other minerals with weak bands, thus mixing spectra and creating broad bands. The sharp bands in the spectrum with the stronger bands seem due to the "sparkly" lustre of the sample (see Figure 1), i.e., an optically smooth surface. In addition, other published laboratory measurements of the fundamental vibrational bands of jarosite in the thermal infrared strongly support our identification of jarosite in Antler and Mineral Park data [10].

Building more inclusive libraries of laboratory spectra could alleviate some of these library-related difficulties. However, the similarity of possible jarosite spectra in different field sites at Mineral Park and Antler (see Figure 2) suggests that libraries of field spectra with proper documentation and analytical verification could be helpful.

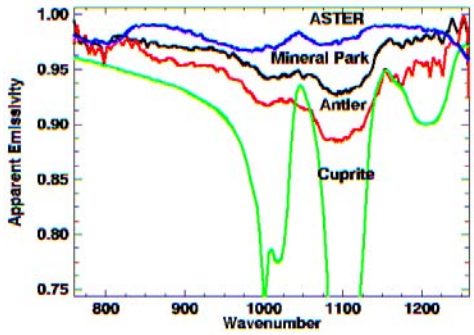

Figure 1: Comparison of possible jarosite signatures from field measurements with library spectra. Upper trace is ASTER library jarosite (125-500µ), next trace is from Mineral Park (Tonka 4801, (44,35)), next trace is from Antler (Tonka 4698, (72, 29)), bottom trace is Cuprite library "sparkly" jarosite crystals on rhyolite. Atmospheric bands cause fine structure in the field spectra.

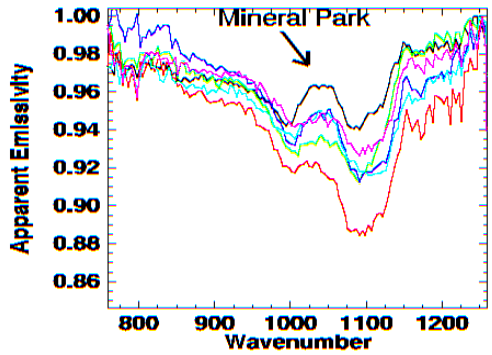

Figure 2: Possible jarosite signatures at Antler and Mineral Park. Upper marked trace is from Mineral Park. All other traces are Antler spectra.

Infrared "Petrography" Results: Spectroscopy studies often are mineralogically-driven, but from a geological perspective it is important to know what rocks are found in association with particular minerals. It has been proposed that jarosite on Mars could have formed by meteoric water-driven pyrolysis of komatiite [11]. If komatiite and jarosite were found near one another on Mars, this hypothesis would gain support.

A kind of infrared "petrography" is possible. Rock-forming silicate minerals have closely spaced Si-O stretch bands in the thermal infrared that interfere in rocks to create broad peaks that are somewhat characteristic. Comparing laboratory spectra of rocks, certain peaks can be associated with particular minerals. Variations in emissivity can indicate the average grain size of particular minerals. The positions of the midpoints of broad bands in igneous rock spectra also seem to correlate with the silica content of the rock.

However, this situation is complicated in the field. Variations in physical properties often change the scattering behavior of geologic materials, producing non-linear effects in rock spectra that could be misinterpreted as mineralogical variations.

In this study, a signature that matches granodiorite was identified at multiple sites at Antler in apparently cobble and boulder-sized rocks of various colors (see Fig. 3) and in yellow soils that appear to cover grey rocks. These rocks tend to have subtler spectral features associated with albite than the laboratory spectra used, but whether this is an effect of initial composition, feldspar weathering, or physical conditions is not known. Sandstone and quartzy dolostone may have been identified in cobble-sized material at Yellow Pine Mine. Sandstone also may have been identified at Alunite in boulder-sized talus in front of a railroad track. Sandstone can be distinguished from laboratory spectra of quartz on the basis of low emissivity and the trapezoidal or triangular shape of at least one of the bands of its principal doublet in the thermal infrared. However, library spectra suggest it may be impossible to distinguish sandstone from sand (weathered quartz) and the metamorphic rock quartzite on these grounds. In other scenes, rock signatures were not present in material that appeared to have similar physical characteristics to the cobble and boulder-sized material at Antler and Yellow Pine. Further fieldwork is necessary to distinguish the spectral effects of physical characteristics from the spectral effects of mineralogy in a variety of igneous, metamorphic, and sedimentary rocks.

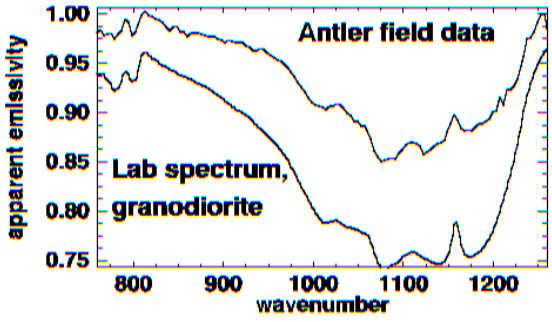

Figure 3: Granodiorite at Antler Upper trace is from Antler (Tonka 4659 (94, 11)), bottom trace is a lab spectrum of coarse granodiorite (H1) from the JHU library.

The Problem of Highly Reflective Minerals: At a site in the Alunite mining district, three layers were apparent in photography: a thick layer of colluvium at the top of the scene, a thinner layer of exposed white minerals, and a layer of talus and reddish-brown soil at the base of the scene. Surprisingly, while the mineral alunite (which is in a Fe-Al solid solution series with jarosite) was identified in the colluvium, the sulfate mineral

gypsum was identified in the white minerals. Close inspection of the photographs of this scene showed that "shiny" (optically smooth) crystals were present in the white minerals. Optically smooth surfaces produced spectra with stronger spectral contrast than rough materials. Library spectra suggested that small amounts of the smooth-surfaced selenite form of gypsum could produce spectra strongly indicative of gypsum, even at small abundance. Conversely, rough surfaces and/or small particle size could prevent the detection of a highly abundant mineral (such as alunite) in the same area.

One lesson from this work is that we could constrain the abundance of gypsum present in the scene only if the spectral contrast of the material is known *a priori*. This is because the abundance is mapped using the spectral contrast of a selected laboratory spectrum.

Alunite and gypsum are both sulfates, but they have slightly different sulfate absorption bands in their emissivity spectra in the 1100-1160 cm^{-1} region. We define the emissivity of those bands as E_{1151} and E_{1111} respectively. Hence, E_{1151}/E_{1111}= the quotient of the weighted sums of the emissivities of the species at that wave number (assuming linear spectral mixing), i.e.

$$\frac{E_{1151}}{E_{1111}} = \frac{(GE_{g1151}) + ((1-G)E_{a1151})}{(GE_{g1111}) + ((1-G)E_{a1111})} \qquad (1)$$

We then use the reference spectra to obtain the emissivities of gypsum and alunite at band number, n, E_{gn} and E_{an}, using the maximum and approximate minimum values in the libraries. We solve to find that:

$$G = \frac{(E_{a2}\frac{E_{1151}}{E_{1111}}) - E_{a1})}{E_{g1} + (E_{a2}\frac{E_{1151}}{E_{1111}}) - E_{a1-(}E_{g2}\frac{E_{1151}}{E_{1111}})} \qquad (2)$$

Using this method, the minimum gypsum abundance in the white minerals ranges from 1.6-11% and ranges from 0-1.6% in the colluvium. Note that the calculation assumes that the gypsum (and alunite) in the field has the same band contrast as the laboratory sample, i.e., has exactly the same surface texture at all scales. If the gypsum observed in the scene has weaker band contrast than the library spectrum used or alunite is not actually present, the actual gypsum abundance may be higher.

Efflorescence: Thin veneers of efflorescent salts (usually calcite or calcium chloride) often are observed on the surface of evaporitic soils [12] [13]. At Antler, photographs showed thin, powdery layers of efflorescent salts in multiple scenes. These efflorescent salts had more featureless spectra than many of the soils or pebble to boulder-sized material in these scenes, and actually could be mapped by their lack of features. What subtle spectral features were present in these salts could be attributed to other materials identified in the scene, which appeared to lie beneath or on the surface of these salts. No calcite was identified in any of the scenes that contained these salts. Possible explanations for the featurelessness of the spectra of these salts are strong cavity effect scattering between the powdery grains of salt or small particle size.

Conclusions: Our methodology mimics some limitations present in studies of Mars because the author was not able to observe the studied sites in the field. It has provided insights into how data from Mini-TES and other infrared spectrometers in extraterrestrial contexts might be analyzed. The primary lessons of this study are: (1) Jarosite and specific types of igneous and sedimentary rocks are identifiable in Mini-TES analog field measurements; (2) The identifiability of minerals of high abundance is not only controlled by their abundance and physical properties but can depend significantly on the physical properties of minerals present in low abundance and *vice versa*; (i.e., abundance mapping based on band depth is a standard method for Mars, but it failed miserably at the Alunite site) and (3) Efflorescent salts do not appear to have identifiable spectral features in the thermal infrared at the Mars analog sites studied but may reduce the spectral contrast of minerals mixed with them.

Further studies of field spectrometer data that are initially unconfirmed by ground truth in sites with other assemblages of minerals that might be on Mars could be valuable, but they are only a first step. Useful confirmatory ground truth for this and future studies would be an investigation of rock and/or soil samples from major photographically similar types of targets that vary spectrally, using petrography, x-ray diffraction, and laboratory spectroscopy in the thermal infrared to confirm the inferred physical, identified mineralogical, and apparent spectral properties of the targets measured in the field. Comparison of this type of detailed ground truth study with the results of a study of the same site without ground truth may be the only way to judge the veracity of current analyses of extraterrestrial data and evaluate new methodologies for analyzing such data without expensive extraterrestrial sample return missions.

Finally, the mapping procedure used in this study differs significantly from the linear mixture modeling conventionally used. It may be necessary to evaluate the usefulness of this method relative to linear mixture modeling, make it more rigorous to allow quantitative comparisons between similar signatures in different scenes, and determine the relationship between confidence and abundance.

Acknowledgements: To L.E Kirkland for being a constant source of inspiration. To N. Rodricks, J. Knoll, and S.A. McBride for being such receptive sounding boards. Thanks to B.T. Greenhagen for taking the photographs and the spectral measurements.

References: [1] Squyres S.W. and Athena Science Team (2004) AAS Meeting 204, #66.01. [2] Greenhagen, B.T., Kirkland, L.E. Grabowski T., and Rainey E.S.G. (2004), *LPSC* XXXV, 1693. [3] Salisbury, J.W. and Hunt, G.R. (1968) AAS Proceedings, 68-038, Vol. 25, AAS Science and Technology Series. [4] Christensen, P.R. et al. (2000) *JGR*, **105** (E4), 9623-9642. [5] ASTER Spectral Library (1999) Jet Propulsion Laboratory, California Institute of Technology, Pasadena, California. [6] Mustard, J.F. and Sunshine, J.M. (1999) in *Remote Sensing for the Earth Sciences*, Wiley, 251-306. [7] Burns, R.G. (1987), *LPSC* XVIII, 141. [8] Long, D.T. et al. (1992), *Chemical Geology*, **96**, 183-202. [9] Benison, K.C. and LaClair, D.A., *Astrobiology*, **3**, 609-618. [10] Adler, H.H. and Kerr, P.F. (1963), *American Mineralogist*, **30**, 133-145. [11] Burns R.G. and Fisher, D.S. (1990), *JGR*, **95** (B9), 14415-14421. [12] Marshall, C.E. (1977), *The Physical Chemistry and Mineralogy of Soils*, Vol. II, Wiley. [13] Tedrow, J.C. (1977) *Soils of the polar landscapes*, Rutgers UP.

TOPOGRAPHIC STUDY OF LARGE MARTIAN IMPACT CRATERS. Jared B. Howenstine[1] and Walter S. Kiefer[2], [1]Dept. of Astronomy, University of Massachusetts Amherst, Amherst MA 01003, jhowenst@student.umass.edu, [2]Lunar and Planetary Institute, 3600 Bay Area Blvd., Houston TX 77058, kiefer@lpi.usra.edu.

Introduction: Improved knowledge of the martian topography enables a quantitative study of large impact structures on Mars. We have measured 42 impact structures, focusing primarily on craters with diameters between 66 and 518 km. The smallest craters in our study allow us to connect our results with previous studies. We also considered large impact basins; Hellas, Argyre, Isidis. Our results show that most large craters on Mars have been filled by a later event and we quantify this fill thickness. Preliminary results of gravity observations of some of these structures provide additional insight into crater structure.

Methods: The Mars Orbital Laser Altimeter (MOLA) experiment has provided an extensive view of the surface topography of Mars [1]. We use a gridded version of the topography in this study. The grid has a horizontal resolution of 64 pixels per degree (930 meters per pixel) and the vertical accuracy is 1-2 meters. Topographic profiles were made using the program Gridview [2].

On each topographic profile we measured the crater's diameter and its rim-to-floor depth. We measured four topographic profiles for each crater: north-south, east-west, northeast-southwest, and northwest-southeast transects through the crater center. This systematic approach to profiling provided eight depth and four diameter measurements for each crater, allowing us to assess the uncertainties in both parameters.

Example topographic profiles are shown in Figure 1. Newton crater has a diameter of 326 km and a depth of 4080 meters. Herschel crater is of a comparable diameter, 297 km, but was measured to have a much shallower rim-to-floor depth, 1450 meters.

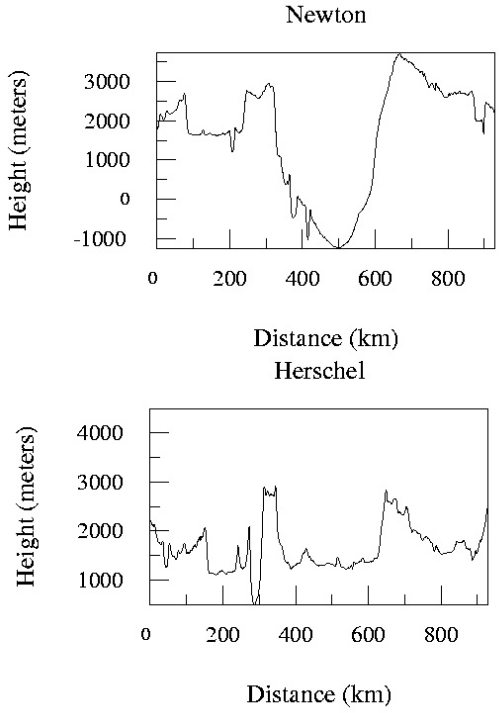

Figure 1: Topographic profiles of craters: (a) Newton crater profiled from south to north along 158 W from 48 S to 32 S, (b) Herschel Crater, south to north along 130 W from 23 S to 7 S.

Topography Results: We follow previous studies of lunar [3] and martian craters [4] by plotting our crater depths versus crater diameters. This process allows us to observe possible power law relationships of the form $d = AD^n$, where d is the rim-to-floor depth in km, D is the diameter in km, and A and n are constants determined by least squares fitting

Figure 2 (last page) shows a broad range of crater depths for a given crater diameter. The deepest craters of a given size are most likely to be pristine, so we fitted the power law to the eleven deepest craters in the size range 66 to 326 km. The resulting power law is $d = 0.44D^{0.38}$, shown as the solid

line in Figure 2. A previous study by Garvin and Frawley produced a power law fit for diameters up to 98 km [6]. Their power fit, (dashed line in Figure 2a) was found to be $d = 0.25D^{0.49}$, Figure 2a. The difference in the two power laws is due to the different range of crater sizes. For the diameter range 66 to 98 km in which the two power law determinations overlap the depth misfit ranges from 214 meters at 66 km diameter to 149 meters at 98 km diameter, which is less than the uncertainty of most of our depth measurements.

Most of the craters larger than 150 km in diameter fall well below the depth expected for their size. These relatively shallow craters have likely been partially filled by sediments or volcanic flows at some time after crater formation. Similarly shallow craters are also known on the Moon [5,6]. Figure 2a can be used to estimate the thickness of this later filling. The craters in Figure 2a have up to 3 km of fill.

Of particular interest is Gusev crater (square in Figure 2a). Gusev may be filled with sediments carried in Ma'adim Vallis [7] and is the landing site of the Mars Exploration Rover 'Spirit.' Our results indicate a fill thickness between 0.8 and 2.2 km at Gusev.

Figure 2b shows our power law extrapolated out to the diameter of some of the largest impact basins on Mars. The power law passes through out error bar for the Hellas basin, although this data point was not used to define the power law parameters. Hellas is known to have some sedimentary fill on its floor [8], but our results indicate that it is thin, with a maximum thickness of 1.1 km. The Argyre and Isidis impact basins have somewhat more fill, 1.6 to 3.6 km for Argyre and 2.2 to 3.5 km for Isidis.

Gravity Results: Gravity measurements of craters studied here show a correlation between topographic infill and reduced gravity anomalies. Figure 3 shows two gravity profiles. Figure 3a is of Newton crater with approximately 170-mGal gravity anomaly. Herschel crater, figure 3b, noted as having a topographic fill-structure, has a maximum of a 70-mGal gravity anomaly. The larger anomaly at Newton is consistent with its greater depth. Quantitative models of these gravity anomalies are currently being developed and are expected to provide constraints on the crustal and lithospheric structure in these regions.

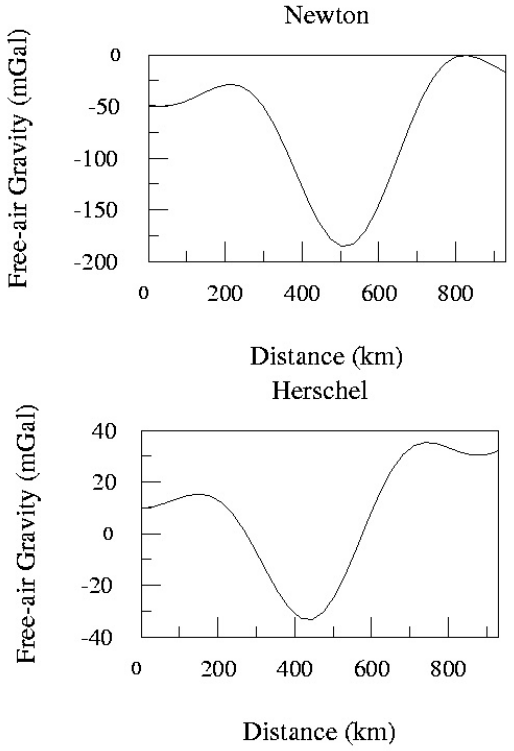

Figure 3: Gravity profile of craters: Same profile south to north for both Newton and Herschel, along same longitude and same latitude range as in Figure 1.

References: [1] Smith et al., *J. Geophys. Res.* 106:23,689-23,722, 2001. [2] Roark et al., *Lunar and Planetary Science 35*, abstract: 1833, 2004. [3] Pike, *Impact and Explosion Cratering*, 489-509, 1977. [4] Garvin and Frawley, *Geophys. Res. Lett.* 25:4405-4408, 1998. [5] De Hon, *Fifth Lunar Conference*, 1:53-59, 1974. [6] Williams and Zuber, *Icarus*, 131:107-122, 1998. [7] Cabrol et al., *J. Geophys. Res.*, 108 (E12): doi:10.1029/2002JE002026, 2003. [8] Leonard and Tanaka, *USGS Geologic Map*, I-2694, 2001.

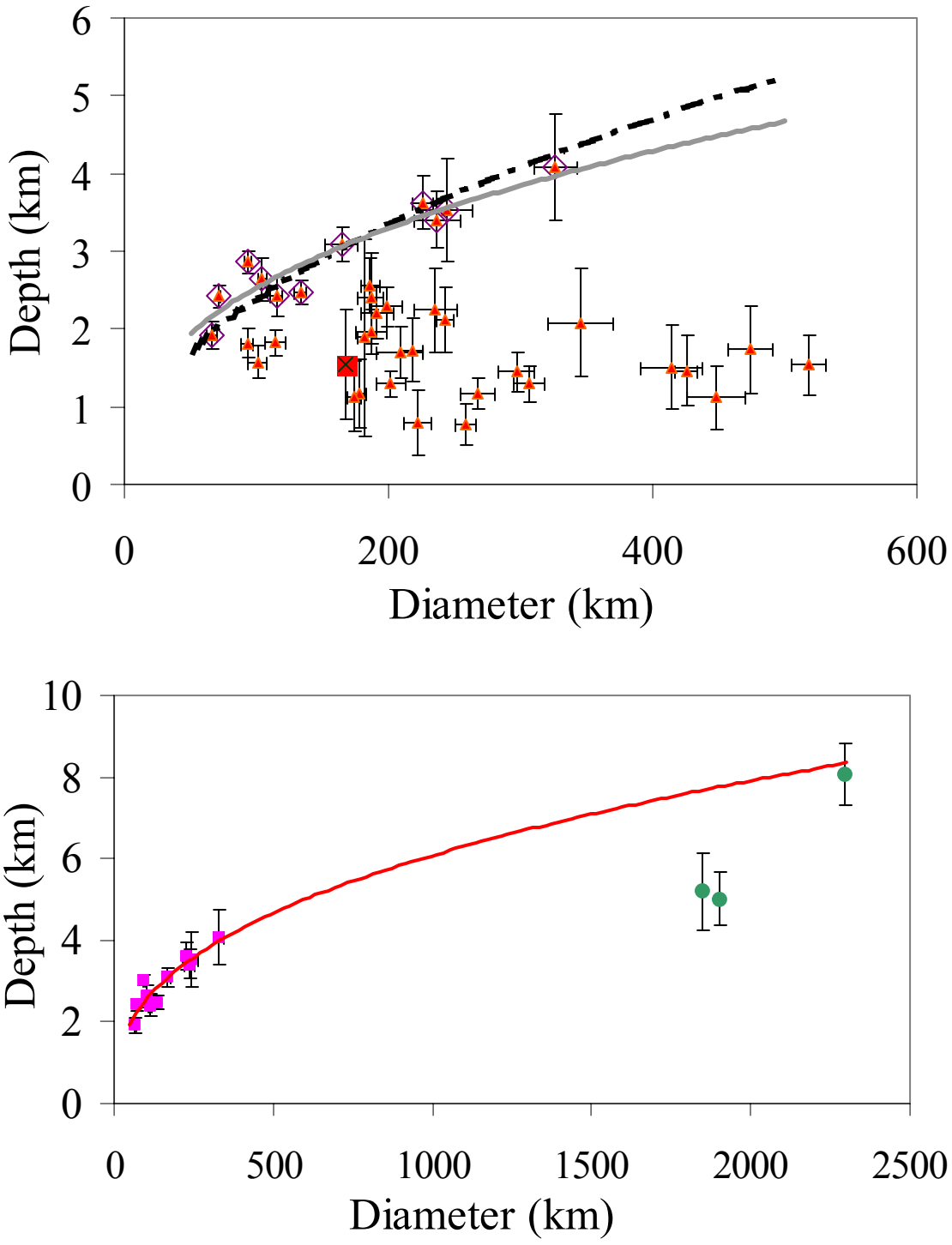

Figure 2: Depth-diameter plots of data: (a) Triangles are data, Diamonds represent data used for power fit of data, Square is Gusev Crater, Dashed line is Garvin and Frawley [4] power fit, Solid line is our power fit. (b) Circles represent 3 largest basins on Mars: Hellas, Isidis and Argyre; Squares are the 11 data points used to define the power law.

SEARCH FOR FLUID INCLUSIONS IN METEORITES AND INITIAL CHARACTERIZATION

Yoko Kebukawa[1] and Mike Zolensky[2]
[1] Earth and Planetary Science, Tokyo Institute of Technology, Tokyo, Japan
email: yoko.soleil@geo.titech.ac.jp
[2] NASA Johnson Space Center, Houston, TX, USA

Introduction: The search for samples of water from the early solar system preserved in asteroid samples will help reveal the origin and role of water in the solar system, including the source of water for early earth, mars and other bodies.

Fluid inclusions are micro-samples of fluid that are trapped at the crystal/fluid interface during growth (primary inclusions) or some later time along a healed fracture in the mineral (secondary inclusions). In the past several years aqueous fluid inclusions have been found in blue/purple halite (NaCl) and sylvite (KCl) found within the matrix of two ordinary chondrite falls, Monahans (1998) (H5) and Zag (H3-6) [1]. And also we have been locating potential fluid inclusions in carbonate minerals in carbonaceous chondrites. Both primary and secondary fluid inclusions are found in Monahans and Zag halite; the latter predominate. The presence of secondary inclusions in the halite indicates that aqueous fluids were locally present following halite deposition, suggesting that aqueous activity could have been episodic. We are not sure that the halite was formed on the H chondrite parent asteroid.

A critical problem has been our inability to verify that the features we are seeing are truly aqueous fluid inclusions rather than other features or contamination. Fortunately this problem can now been addressed with the new Raman Microprobe we have just installed at JSC. With this new instrument we can for the first time non-destructively analyze water and other aqueous fluids within meteorites.

Experimental Methods: Samples are CI chondrite (Ivuna), Ordinary chondrite (Amgala) and Tagish Lake. CI chondrites are from primitive, water and organic bearing asteroids, probably C asteroids. Ordinary chondrites are more typical of the majority of asteroids, the S asteroids. Tagish Lake is probably from a D asteroid [2].

Samples are separated grains of carbonates and halite. Grains containing fluid inclusions are selected under a petrographic microscope and characterized by a Jobin Yvonne Ramalog Laser Raman Microprobe which can be used to characterize of minerals and water.

Results: Features that could be fluid inclusions were found in transparency grains (Ca-Mg-Fe carbonates) of Ivuna (CI2) and Tagish Lake (Figure 1). But we have been unable to find one containing a liquid with a moving vapor bubble. As of the writing of this abstract we are still searching.

On the other hand, we found numerous new fluid inclusions with a liquid and a moving vapor bubble in Zag halite (Figure 2). We examined these by laser Raman microprobe, but have not been able to see spectral peaks for water, probably because these inclusions are so small.

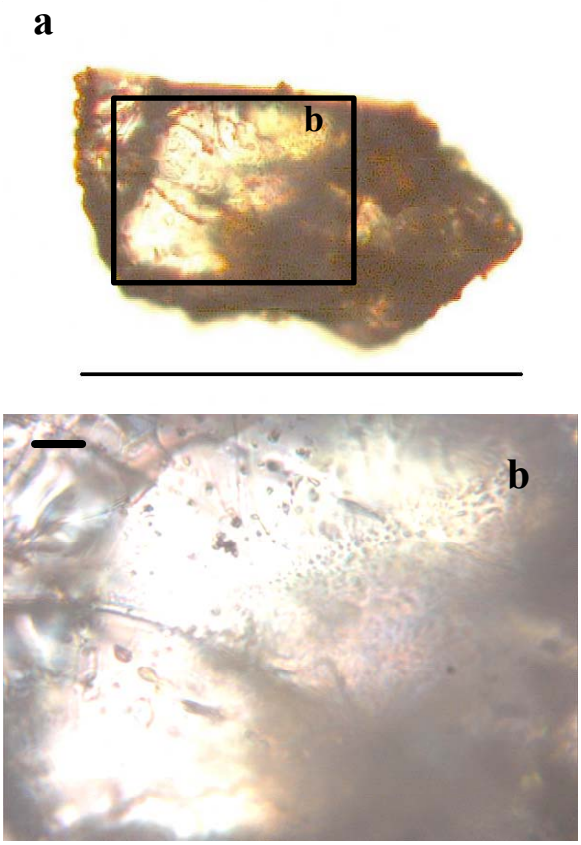

Figure1: Transmitted light image of Tagish Lake. Scale bar, a: 200 m, b: 5 m.

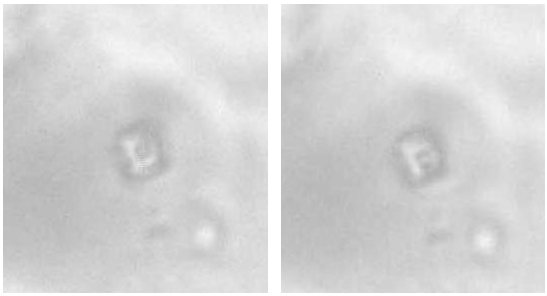

Figure2: Transmitted light image of Zag halite. Primary inclusion containing a liquid and a moving bubble. Inclusion is approximately 2.5 m in diameter. Note movement of bubble between separate photos.

Discussion: As yet I have not found any verifiable aqueous fluid inclusions with a liquid and a moving bubble in these meteorites. We think that we can obtain good spectra of water in the Zag halite if we have time to determine optimum conditions of laser energy, filters and so on.

Conclusions: The search for samples of water from the early solar system preserved in asteroid samples will help reveal the origin and role of water in the solar system. Samples are fine powder of Ivuna (CI2), Tagish Lake and Amgala (H5). Features that could be fluid inclusions were found in Ivuna and Tagish Lake. When examined by laser Raman microprobe, we could not verify the presence of aqueous fluids in these. Potential fluid inclusions with a liquid and a moving bubble were found in Zag (H5), but analysis by Raman microprobe did not verify the presence of water.

References: [1] Zolensky M.E., Bodnar R.J., and Rubin A.E. (1999) Asteroidal Water Within Fluid-Inclusion-Bearing Halite in Ordinary Chondrites. *Meteoritics and Planetary Science, 34,* in press. [2] Hiroi T., Zolensky M.E. and Pieters C.M. (2001) The Tagish Lake Meteorite: A Possible Sample from a D-Type Asteroid. *Science, 293,* 2234-2236.

Prospecting for Martian Ice. S.A. McBride[1], C.C. Allen[2], M.S. Bell[3], [1]Cornell University, Ithaca, NY, [2]NASA Johnson Space Center, Houston, TX, [3]Lockheed Martin @ Johnson Space Center, Houston, TX.

Introduction: During high Martian obliquity, ice is stable to lower latitudes [1,2] than currently predicted by stability models and observed by the Gamma Ray Spectrometer (~60°N) [3]. An ice-rich layer deposited at mid-latitudes could persist to the present day; ablation of the top 1 m of ice leaving a thin insulating cover of dust could account for lack of its detection by GRS. The presence of an ice-layer in the mid-latitudes is confirmed by a network of polygons, interpreted as ice-wedge cracks [4,5]. This study focuses on an exceptional concentration of polygons in Western Utopia (section of Casius quadrangle, roughly 40°-50°N, 255°-300°W) [6]. We attempt to determine the thickness and age of this ice layer through crater-polygons relations.

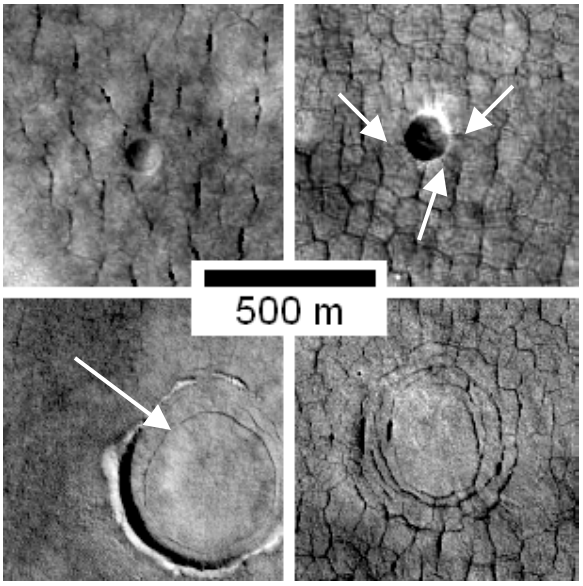

Figure 1 – Crater morphologies in relation to polygonal fractures as seen in MOC images (clockwise from top left): fresh (R0301150); radial cracks (M0401631); concentric cracks (R0502250); inner wall cracks (R0501314).

Methods: Using a list of frames containing polygons [7], we completed a survey of craters within 9120 km^2 of polygonal terrain in all narrow angle MOC images in the latitudes 30°-65°N released between 09/97 and 09/03 [8]. 72% of these polygons are in the Casius quadrangle. For the 687 craters with a diameter between 100 m and 4 km we recorded location, diameter, and crater morphology: fresh, radial cracks, concentric cracks, or inner wall cracks (Figure 1). Fresh craters appear younger than polygons as they are not cross-cut by any cracks. Radial cracks around a crater are interpreted as cracks forming in relation to the free face of the inner crater wall. Concentric cracks are circular rings of cracks in an otherwise normal polygonal network. Inner wall cracks are similar to concentric except they form in craters with rims still protruding. The presence or absence of thermokarst and the density of craters smaller than 100 m were also noted.

Thickness of the ice layer: Many craters are only visible as concentric cracks in an otherwise random polygon network. The pattern of ice-wedge cracking appears to be controlled by an underlying crater rim or fractures associated with cratering. There appears to be a diameter dependent boundary between such concentric cracks, and inner wall cracks forming around a still-protruding rim. Apparently craters up to a certain size have been buried by the ice rich layer, while larger craters have not. The largest buried crater has a diameter of 1.12 km, while the smallest partially buried crater with a protruding rim has a diameter of 0.46 km. The diameter of the smallest craters with protruding rims shows a slight increase with latitude (Figure 2).

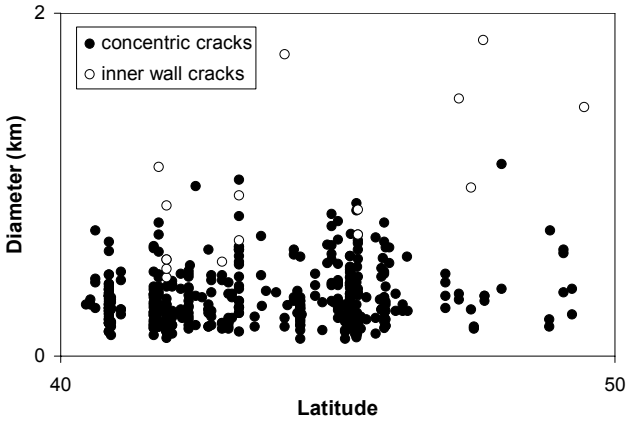

Figure 2 – Crater morphology by size and latitude showing diameter-dependent transition.

A sharp decline in the density of very small craters (< 100 m) northwards suggests they are being degraded or buried. Mantling has been suggested to have recently operated in the northern plains [1,9]. The diameter dependent morphology transition of craters supports this hypothesis, and provides a method of gauging the thickness of the mantle. As the crater may be a preferred site of deposition of ice and dust, the rim height rather than the depth is a better parameter to use for crater burial. Using the global average relation for simple craters derived from MOLA topography, $h_{rim}=0.04D^{0.31}$ [10], the mantling ice is 31 to 41 m thick. As this expression

for rim height is for all Martian craters, including partially buried ones, the calculated thickness represents a minimum value. The unknown nature of the target and state of crater degradation in this specific region increases the uncertainty of this thickness.

Age of the ice layer: 97% of craters observed in the Casius quadrangle predate polygon formation, suggesting a very young age for the ice. A more quantitative absolute dating system has been developed for Mars [11]. Ages obtained by crater density for units on the Moon have been calibrated by radiometrically dated samples returned by the Apollo missions. By adjusting the incoming bolide flux for Martian gravity, orbit, and atmosphere, this system can be applied to Martian geologic units. According to these crater density isochrons (Figure 3), polygons were forming until between 0.5 and 10 Ma. As many of the apparently fresh craters are ambiguous this is more of a maximum age.

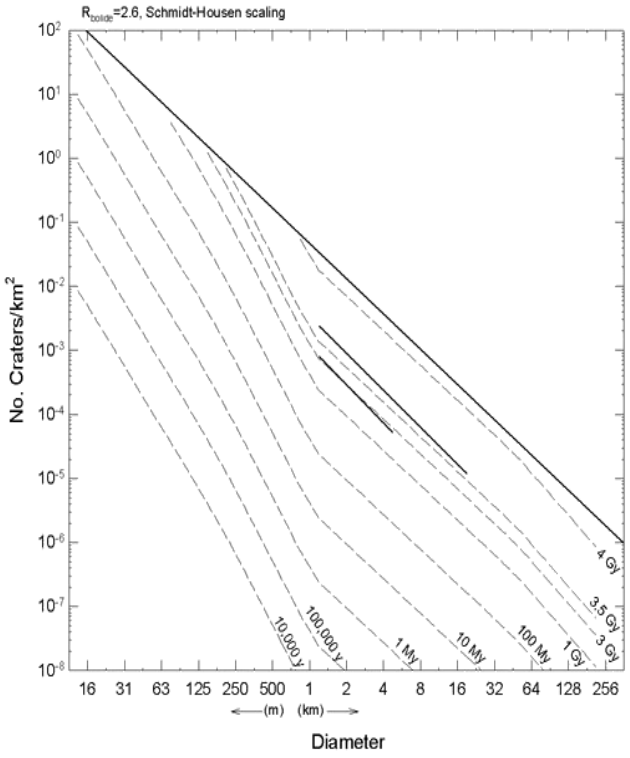

Figure 3 – Density distribution for craters associated with polygons in the Casius quadrangle, as well as all craters > 3 km [12]. Isochrons from [11].

Fresh and radially cracked crater abundances suggest that the mantling unit stopped forming between 5 to 50 Ma, older than the last high obliquity cycle. Mars has greater fluctuations of obliquity than the Earth, including regular oscillations as well as a generally higher level of obliquity before 5 Ma [13,14]. Isochrons [11] suggest the formation of the majority of the blanket before the drop to present obliquity ranges at 5 Ma, as in [2,14]. Perhaps mantling occurs in the high amplitude part of the obliquity oscillations, and was magnified before 5 Ma.

All craters, including those seen only as concentric rings of polygons, align well with a count done for larger craters (D = 3-80 km) that gave a Hesperian-Amazonian age. The apparent downturn of the crater catalog below 5 km is likely due to omission of craters [12]. However, the decreasing density of craters from this study smaller than 1 km appears robust, again suggesting a mantle burying craters up to this size.

Nature of the ice layer: The survey also revealed some related trends in ice-associated features. Most polygons north of 60°N are light relative to their surroundings, while most south of 60°N are dark. Thermokarst in the polygons is present mostly between 40°-50°N, mostly in the northern half of this range. Indicators of climate change included widening polygons (Figure 4), polygons on thermokarst (Figure 5), mantled thermokarst (Figure 6), and layered thermokarst scarps (Figure 7).

The polygons scattered across the rest of the northern plains differ considerably from the Casius concentration. The polygons are in general wider and less well defined. On average the crater distribution matches the Casius quadrangle; however, some areas have the appearance of being much older due to extensive cratering. The global diameter dependent transition from concentric to inner wall cracks matches with the Casius quadrangle.

Conclusion: An ice rich layer approximately 40 m thick is revealed by the presence of recently active ice-wedge polygons in at least part of the Casius quadrangle, and possibly more extensively across the northern plains. Higher obliquity probably caused deposition of the mantle before 5 Ma; formation of polygons has continued until the present.

Acknowledgements: Lisa Kanner for her list of MOC images containing polygons; Nadine Barlow for her crater catalog of the Casius quadrangle; and Susan Sakimoto for guidance on crater morphology.

References: [1] Head J.W. et al. (2003) *Nature*, 426, 797-801. [2] Kreslavsky M.A. and Head J.W. (2004) *LPSC XXXV*, Abstract #1201. [3] Boynton W.V. et al. (2002) *Science*, 297, 81-85. [4] Seibert N.M. and Kargel J.S. (2001) *Geo. Res. Lett.*, 28, 899-902. [5] Mellon M.T. (1999) *LPSC XXX*, Abstract #1118. [6] Kanner L.C. et al. (2004) *LPSC XXXV*, Abstract #1982. [7] Kanner L.C. (2004) *personal*

contact. [8] Malin M.C. et al. (1997-2003) *Malin Space Center Systems Mars Orbiter Camera Image Gallery* (www.msss.com/moc_gallery). [9] Kostama V.P. et al. (2004) *LPSC XXXV*, Abstract #1203. [10] Garvin J.B. et al. (2003) *SICM*, Abstract #3277. [11] Hartmann W.K. et al. (2002) *Planetary Science Institute* (www.psi.edu/projects/mgs/isochron.html). [12] Barlow N.G. (2004) *personal contact*. [13] Laskar J. et al. (2004) *LPSC XXXV*, Abstract #1600. [14] Manning C.V. et al. (2004) *LPSC XXXV*, Abstract #1818.

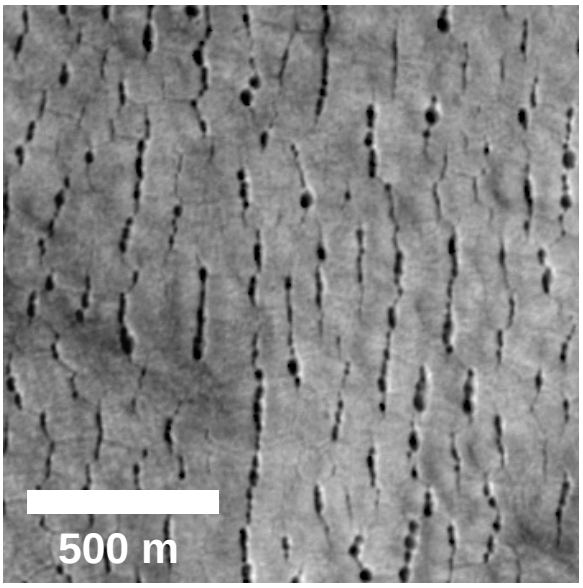

Figure 4 – Widening polygonal cracks (E0200880)

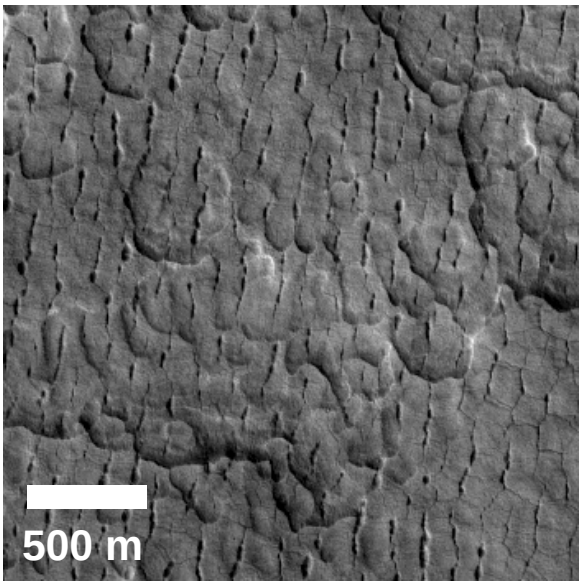

Figure 5 – Polygons on thermokarst (R0501736)

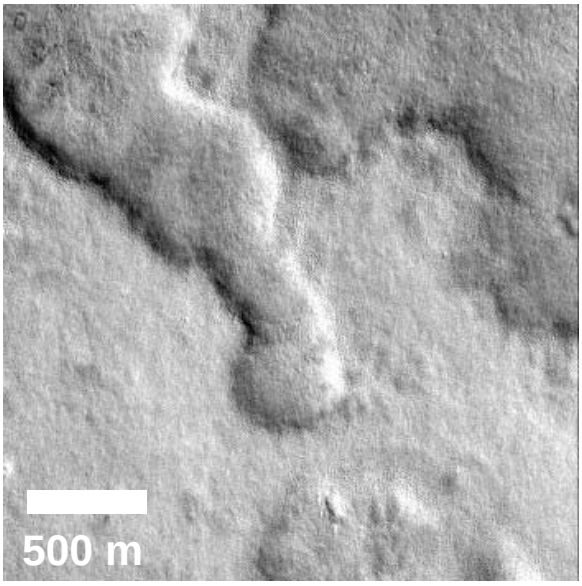

Figure 6 – Mantled thermokarst (R0501783)

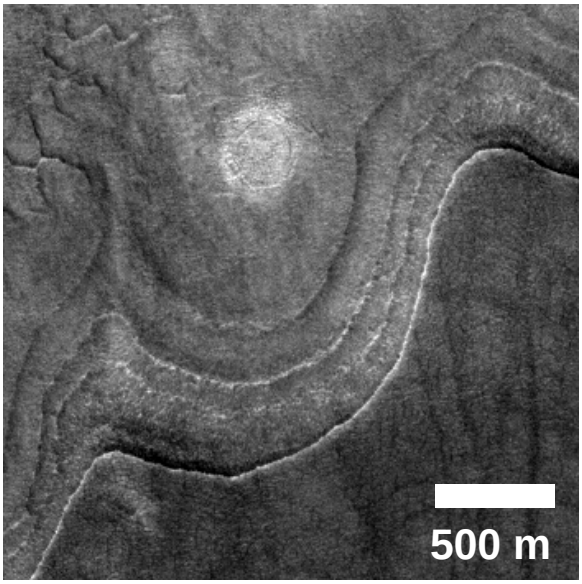

Figure 7 – Layered thermokarst scarp (E1600139)

IRON METAL SPHERULES FOUND AT DEEP-SEA HYDROTHERMAL VENT.

Táhirih Motazedian, Carl Allen, Kelly Snook. NASA-JSC, Houston, TX 77058.

Introduction: Metal spherules were found on a rock retrieved from the Menez Gwen hydrothermal vent fields (37º50'N on the Mid-Atlantic Ridge) [1], at a depth of 840m. This site was discovered in 1994 and lack of significant alteration indicates that hydrothermal activity has begun only recently. The water temperature at this site is around 278°C, and it is known to be a highly oxidizing environment. Menez Gwen lacks a central rift valley, which is unusual for marine hydrothermal vent sites. Instead, it has an axial graben with a young volcano in the northern section. Active anhydrite chimneys are found on the western flank of the volcano, and 'rusticles' are found in abundance in the area. Rusticles look similar in form to stalagmites, but they are made as bacteria mine the organic elements out of metallic iron or steel [2].

The rock used for this study (known as 'Cranberry Rock') was taken from a rusticle field nearby the Menez Gwen hydrothermal vents. The larger rock (which will be referred to as the 'mother rock') from which Cranberry rock was taken is a large boulder of hydrothermally altered basalt.

Cranberry rock (Figure 1) originally housed a fascinating layer of spherules embedded on one surface of the rock. Just above the spherule layer the rock was coated with an orange-yellow sulfurous layer, while the inside of the rock was dark grey. The rock still bears these characteristics, but air exposure has oxidized the rock so that almost the entirety of the spherule layer has weathered away, leaving behind a heap of loose spherules (Figure 2).

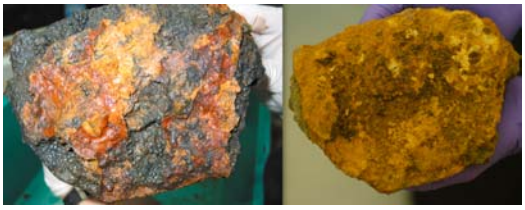

Figure 1: Top spherule layer of rock. On the left, the top surface of the rock when it was first retrieved from the ocean. On the right, the top surface of the rock a year after retrieval.

Figure 2: Loose spherules, as well as a small chunk of the spherule layer with spherules still embedded in it.

We decided to call the spherules 'cranberries' because of their red color and because of the intriguing similarities between our spherules and the 'blueberries' found at Meridiani Planum on Mars [3].

Observations and Analyses: The rock was cut in half and a slab was sliced off from the freshly exposed inner surface of the rock. Thin sections were made from this slab to capture a cross section of the rock, from top to bottom. Analyses of the thin sections have been performed using SEM, microprobe, XRD, Raman spectroscopy, as well as an optical microscope. Microprobe and XRD results show that the grey matrix of the rock is a basalt that has undergone

hydrothermal alteration. It bears an abundance of tabular barite crystals.

These spherules are remarkably uniform in size and sphericity. The mean diameter is consistently between 2.5 to 3mm. The spherules, when exposed, are a shiny metallic silver color and are *extremely* hard. After having been exposed to over one year of open-air exposure, however, they are now always encased in a weathering rind that consists of a dull black layer coated by a very thin orange-brown layer. The thickness of the weathering rind varies greatly, and some spherules have been oxidized completely to the core. Such spherules break apart upon the slightest prodding—unlike the average spherule, which is difficult to cut with a saw. The spherules are perfectly spherical except when pieces of the weathering rind have broken off.

Many spherules have tunnel-like cavities that lead into their centers (Figure 3). Some spherules are conjoined, and they intersect one another in such a way that they appear to have grown together.

Figure 3: Spherule with hole and crack.

Microprobe, XRD, and Raman results show that the spherules are made of native iron (Fe^0). The weathering rind, according to Raman spectra, appears to be composed of hematite. This observation is compliant with the findings of Costa et al. [1], which state that alteration minerals in the Menez Gwen hydrothermal site are mainly amorphous iron oxides.

Microscopic observation of the thin sections has shown that some spherule surfaces are covered with very peculiar pod-like structures (Figure 4) that are composed almost entirely of Fe and Cl. No speculation has yet been made as to the origin or of these features.

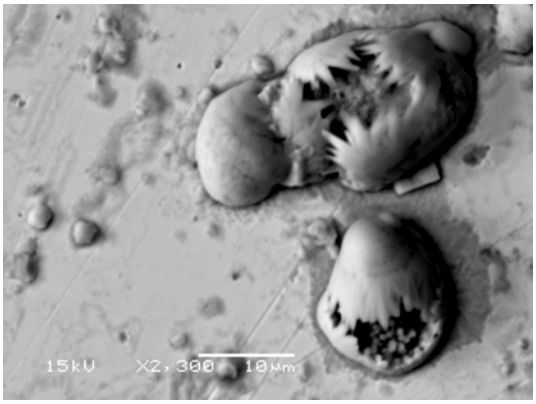

Figure 4: Some of the strange pod-like structures found on spherule surfaces under SEM.

Theory: Pure iron metal is exceedingly rare on Earth and is usually of meteoric origin (and thus contains Ni). There is no trace of Ni detected thus far in the spherules, so an extraterrestrial origin for these spherules is unlikely. On earth native iron is known to form in only a few natural settings. The largest occurrence of terrestrial native iron exists in the Disko Island basalts of West Greenland [4]. Native iron forms here from the intrusion of mantle-derived magmas into carbonaceous sediments. The magma assimilates carbon as it intrudes into the sediment, and this carbon reduces iron oxides present in the magma to form native iron.

In this case we are suggesting that the Menez Gwen volcano has produced iron-rich magma that has interacted with surrounding carbon-rich sediments to form the iron metal we observe. The iron was encased inside a pillow of basalt so that it was never exposed to the oxidizing seawater. This theory is in accordance with the findings of Costa et al. [1], who observed the preservation of massive sulfide deposits at the Menez Gwen site. They found that sulfides were being protected from oxidation through the means of an insulating rock cover known as "slab rock," which shields the sulfides from exposure to seawater. Surveillance of the video footage of the Cranberry rock excavation showed that the spherules on the rock were indeed embedded inside the larger rock.

It is not yet understood why the iron metal should form uniform spherules, though it has been loosely speculated that these spherules may be nucleated by some form of microbial life.

The presence of rusticles at Menez Gwen holds intriguing implications for the production of iron metal in this hydrothermal environment. Rusticles have only ever been observed to form on man-made iron structures, because of the rarity of natural sources of iron metal at the bottom of the ocean. Therefore the abundant presence of rusticles at Menez Gwen suggests the possibility that the cranberry spherules are not the only iron metal being produced at this site.

Mars Analog: The iron spherules we are seeing from the Menez Gwen site appear to be a plausible analog for the hematite spherules we find on Mars. At Menez Gwen we begin with iron metal spherules formed in a deep-sea environment, which then alter to hematite when exposed to the atmosphere. It is possible that the same process has occurred on Mars to form the blueberries we find there. Iron metal spherules could have formed at the bottom of a great lake or ocean on Mars, and these spherules could have transformed to hematite after removal from the water.

Acknowledgements: I would like to extend my gratitude to Dave McKay, Charlie Galindo, and Mike Zolensky for their kind assistance, and to James Cameron for making it all possible.

References: **[1]** Costa I. et al. (1995) *Memórias no. 4, Universidade do Porto - Faculdade de Ciencias, Museu e Laboratório Mineralógico e Geológico,* p. 979-983. **[2]** Pellegrino C. and Cullimore R. (June 1997) *Voyage*. **[3]** Squyres S.W. et al. (2004) *LPSC XXXV, Abs. #2187.* **[4]** Goodrich C.A. (1984) *LPSC XV Proceedings.*

AN INFRARED SPECTROSCOPY AND ELECTRON MICROSCOPY STUDY OF ANTARCTIC MICROMETEORITES: MINERALOGY AND ORGANIC MATTER.

Akiko Suzuki
Department of Earth and Planetary Sciences, Faculty of Sciences, Kyushu University, Japan.

Advisor: Lindsay P. Keller
Mail Code: SR, NASA Johnson Space Center, Houston, TX 77058.

Introduction: Micrometeorites extracted from Antarctic ice are a major source of extraterrestrial materials available for study in the laboratory. Materials in this size range are important because the peak in the mass flux distribution of extraterrestrial particles accreted by the Earth occurs for particles ~200 m in diameter with a mass accretion rate estimated at ~40x10^6 kg/year [1]. It has been suggested that micrometeorites may have contributed much pre-biotic organic matter to the early Earth [2], but the types and abundance of organic material in micrometeorites is poorly known. We have undertaken a study of small micrometeorites (50-100 m) in order to determine the types of organic matter that is present in the particles and to estimate the abundance. We also want to compare our results to earlier work on large IDPs (20-50 m) and on large micrometeorites (100-400 m).

Samples and Methods: The micrometeorite samples were selected from a bulk sieve sample of 50-100 m diameter particles extracted from Antarctic "blue" ice near Cap-Prudhomme [3, Sample vial 15-18-50A]. We used a tungsten needle to pick individual particles and transfer them to a scanning electron microscope (SEM) mount – the selected particles include micrometeorites (both melted and unmelted) and terrestrial particles such as quartz grains, rust particles from the ice melting procedure [4], and penguin feathers. The particles were placed on polished carbon plates coated with a thin film of CrystalBond adhesive, carbon-coated and analyzed in a JEOL 5910LV SEM. For each particle, we collected a secondary electron image and energy-dispersive X-ray (EDX) spectra to select particles with approximately chondritic bulk compositions. Following the SEM analysis, the micrometeorites were removed from the SEM mount, washed in acetone to remove the CrystalBond residue, and crushed between sapphire plates. The crushed material was pressed into polished plates of KBr for infrared spectroscopy analysis. We used a Thermo-Nicolet Continuum microscope for the Fourier-transform infrared (FTIR) analyses. For the FTIR spectra, 100-500 individual scans were obtained in transmission mode using a 150 m x 150 m field-limiting aperture and a liquid nitrogen cooled HgCdTe detector sensitive over the 4000-400 cm^{-1} spectral range. FTIR spectra were also collected from several pure mineral standards and meteorite matrix samples (Tagish Lake, Murchison, and Allende). Several of the terrestrial contaminant particles were analyzed in the same manner as the micrometeorite samples as control samples.

Results and Discussion: We analyzed a total of 12 micrometeorite particles and divided them into 4 groups based upon their silicate mineralogy as inferred from their FTIR spectra (Table 1). The 4 groups we defined are pyroxene-rich, olivine-rich, mixed olivine-pyroxene and clay-rich. Our defined groups are consistent with previous work [5, 6], but there are differences in the population statistics on the distribution of the micrometeorites among the groups. While we observe similar numbers of pyroxene-rich and olivine-rich particles, other studies [5,6] show that olivine-rich particles are 2-3X as abundant as the pyroxene-rich group. We also observe a higher percentage of unmelted clay-rich particles (2 of 12) compared to Nakamura et al. (3 of 56) and Alexander et al. (0 out of 20). Weak features due to C-H stretching vibrations in aliphatic hydrocarbons are detected in all of the particles except one olivine-rich particle. The C-H feature (in the 2800-3000 cm^{-1} region) is strongest in the pyroxene-rich particles, but the relative intensity (compared to the strength of the silicate feature) shows that the abundance of aliphatic hydrocarbons is lower in the micrometeorite samples compared to the ratio observed in interplanetary dust particles (IDPs) [7].

Sample	Avg. Dia.	Mineralogy	C-H feature
MMGR6	113	oliv	v. weak
MMGR8	105	pyx	medium
MMGR9	130	ol-pyx	not detected
MMGR11	142	pyx	medium
MMGR12	110	ol-pyx	v. weak
MMGR16	115	pyx	medium
MMGR19	102	oliv	v. weak
MMGR20	80	sap	strong
MMGR21	73	ol-pyx	v. weak
MM13	120	serp	medium
MM12	95	oliv	v. weak
MM10	110	oliv	v. weak

Table 1. Average diameter, major mineralogy and relative intensity of the C-H feature in the FTIR spectra. (oliv,ol=olivine, pyx=pyroxene, sap=saponite and serp=serpentine).

Conclusions: Despite strong atmospheric heating, we observed indigenous organic matter in all but one of the analyzed particles. Detectable organics in the micrometeorite samples consisted of aliphatic hydrocarbon whose abundance is intermediate between IDPs and carbonaceous chondrite meteorite matrix. The pyroxene-rich and clay-rich particles showed the highest abundance of aliphatic hydrocarbons – this result is consistent with previous work showing that entry heating converts the clay minerals in clay-rich micrometeorites into pyroxene.

Acknowledgements: This work was supported by a Lunar and Planetary Institute (LPI) Internship to AS and by NASA RTOP 344-31-40-07 to LPK.

References: [1] Love, S. G. and Brownlee, D. E. (1993) *Science*, 262, 550. [2] Anders, E. (1989) *Nature*, 342, 255. [3] Maurette, M. (1994) [4] D. Brownlee, pers. Comm. [5]

Nakamura, T. *et al.* (2001) *GCA*, 65, 4385. [6] Alexander, C. M. O'D. *et al.* (1992) *LPSC XXIII,* 7. [7] Flynn, G. J. *et al*. (2003) *GCA*, 67, 3224.

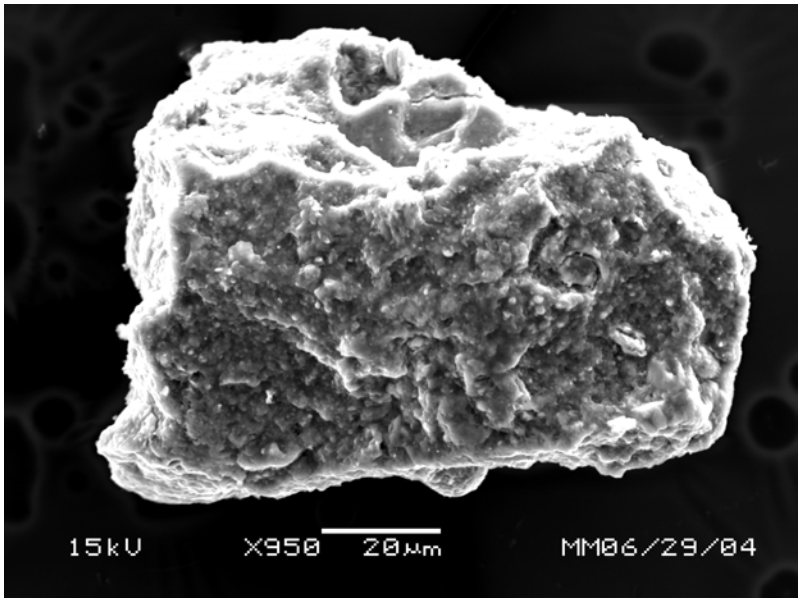

Figure 1. Scanning electron microscope image of olivine-rich Micrometeorite MMGR6.

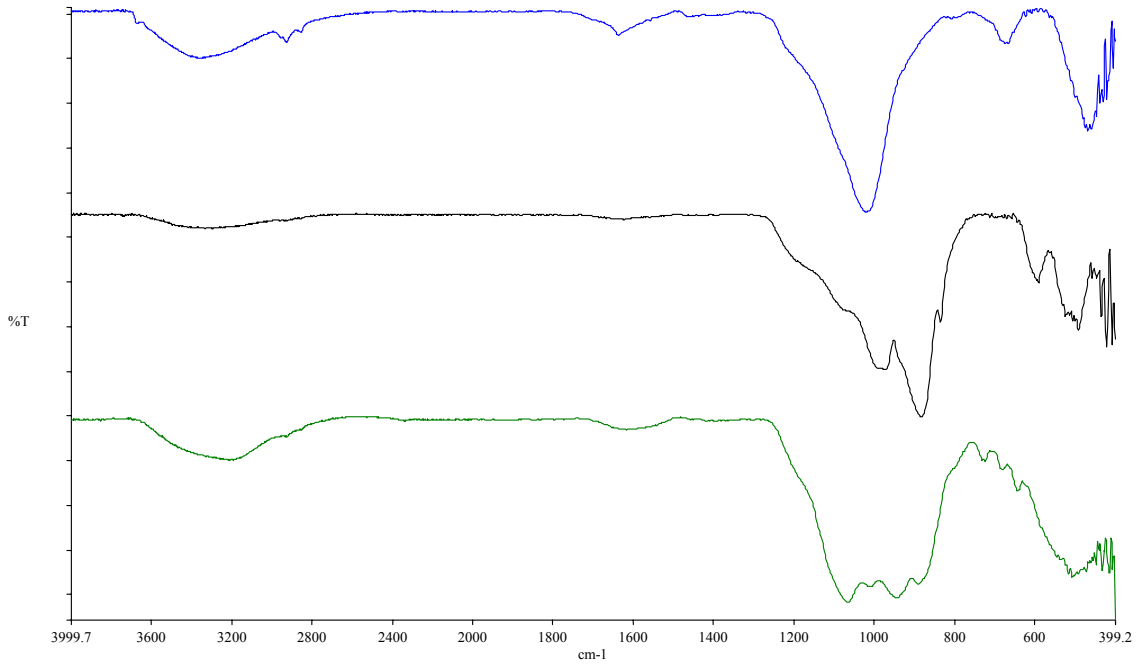

Figure 2. FTIR transmission spectrum of a clay-rich micrometeorite (MM) (top, MM20), an olivine-rich MM (middle, MM6), and a pyroxene-rich MM (bottom, MMGR11),